FINAL REPORT

Estimation of changes in snow cover and glacier mass balance for Upper Chenab River Basin

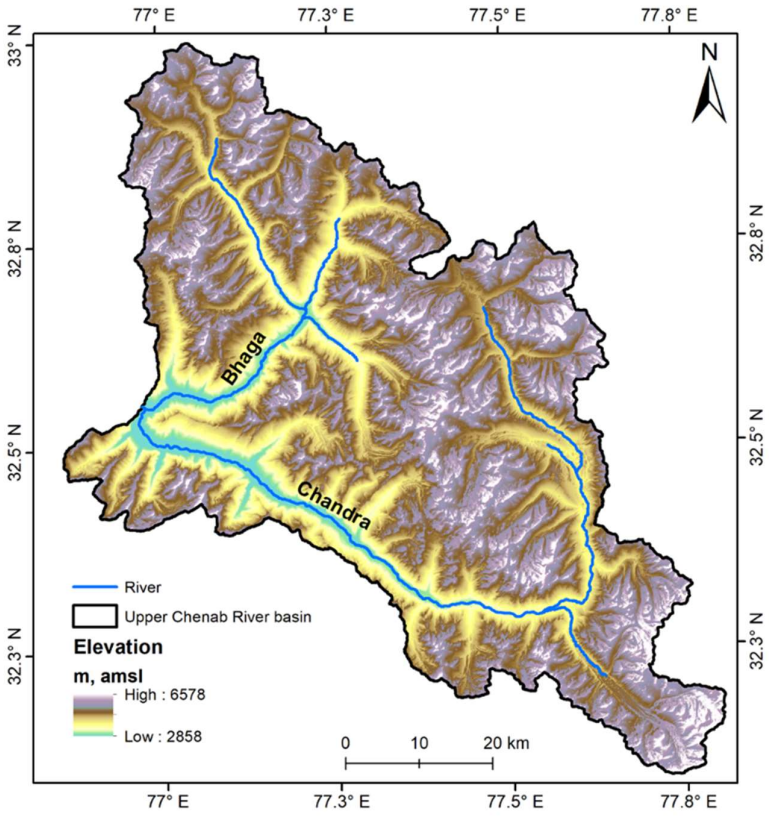

NATIONAL INSTITUTE OF HYDROLOGY
Western Himalayan Regional Centre, Jammu

MARCH 2025

FINAL REPORT

Estimation of changes in snow cover and glacier mass balance for Upper Chenab River Basin

NATIONAL INSTITUTE OF HYDROLOGY
Western Himalayan Regional Centre, Jammu

MARCH 2025

Director : Dr. Manmohan Goel
Coordinator : Dr. Surjeet Singh

STUDY GROUP

Principal Investigator (PI)	**:**	**Dr. P. G. Jose, Scientist 'E' & Head**
Team (Co-PIs)	**:**	**Dr. D. S. Bisht, Scientist 'C'**
		Dr. Sachchidanand Singh, Scientist 'B'
		Dr. Riyaz Ahmad Mir, Scientist 'C'
		Mr. Ankit Khajuria, Resource Person (Jr.)
		Ms. Priyanka Verma, GIS Analysist
		Mr. Girish Raina, GIS Analysist

CONTENTS

CHAPTER 1

INTRODUCTION

1.1 Background

Human influence has warmed the climate at a rate that is unprecedented in at least the last 2000 years resulting in diverse negative impacts including rising temperatures, altering precipitation patterns at spatial and temporal scales and glacier retreat. The observed greenhouse gas warming, driven by emissions from human activities, is partly masked by aerosol cooling. Human influence has proven to be the main driver of the hot extremes, which have increased in frequency as well as intensity in the 21st century, apart from the observed decrease in frozen areas in various parts of the planet and resulted in the global retreat of glaciers since 1990 and a decrease in spring snow cover since 1950 (Hock et al, 2019). Immerzeel et al (2020) analyzing the importance and vulnerability of the world's water towers, concluded that the most critical water towers in terms of their role in sustaining water demand, are also the ones that are most vulnerable. Progressing glacier melt and the associated lakes raises the threat of glacier lake outburst floods (GLOFs), while declining melt water supply changes the hydrological regime, resulting in changing water availability, especially during dry seasons (Motschmann et al, 2020).

Himalaya, the abode of snow and ice has stood as the guardian of the South Asian sub-continent protecting it for several millennia from the extremes of weather and birthing civilizations and biodiversity hotspots that are among the best globally. Witnessing many a cycle of global climate fluctuation and resultant glacier retreats and advances, this sentinel of our motherland has borne the brunt of harsh winds from the north to protect and nurture a thriving and ever-evolving socio-cultural human ecosystem. While glaciers and transient snow cover a large proportion of the Himalayan landscape, these are impacted by its geo-climatic setting, the altitude of its mountain ranges and proximity to the Indian Ocean and the resultant annual cycles of solid precipitation and melt. This interplay of snow accumulation and melt at various scales and significance sustains the perennial flow of the mighty Himalayan river systems Indus, Ganga and Brahmaputra.

Although the impact of cryospheric components on the water resources of mountainous regions has been recognized globally, it is not well understood in the Himalayan region for various reasons. For one, the Himalayan glaciers are found at altitudes above 4000 m asl in very rugged and challenging terrains. Although there are reportedly 10,000 odd glaciers covering approximately 100,000 Km^2 in the Indian Himalayan Region (IHR), only a handful have been studied to merit inclusion in global estimates that report that these are receding at rates comparable to other glaciated regions in the world. The longest glaciological mass balance record from India (Wagnon et al., 2007; Azam et al., 2012; Vincent et al., 2013; Azam et al., 2019; Mandal et al., 2020) gave a cumulative wastage of -7.87 m.w.e.a^{-1} for Chhota Shigri Glacier, Chandra sub-basin, Chenab basin, Himachal Himalaya. An analysis of glacier changes from 1979 to 2016 on Kolhai Glacier using multi-temporal topographic and remote sensing data revealed that the glacier lost an area of $13.63 \pm 2.3\%$ (1.74 ± 0.023 km^2) at a rate of

$48 \pm 0.63\ m^2a^{-1}$, with the area loss increasing in the 21st century (Mir, 2018). Preliminary studies on the impact of deglaciation using tracer experiments has been carried out in the ablation zones of Dokriani and Gangotri glaciers (Hasnain et al., 2001; Pottakkal et al., 2014) suggesting significant role played by melt water entering the glacier body in accelerating the seasonal evolution of glacier hydrological system and influencing not only the release of meltwater at the glacier terminus, but also the glacier dynamics. Theyyan and Gergan (2010) conceptualized three different glacier catchments in the Himalayan region having different behavior. A recent remote sensing based estimation of snow line elevation over a span of 19 years (2003–2021), observed a notable reduction in the mean annual permanent snow zone area, decreasing by -2.61 %, -2.37 %, and -4.18 % from winter (DJF) to summer (JJA) in Upper Indus, Ganga and Brahmaputra respectively (Dixit et al, 2024).

Racoviteanu et al. (2008) gives an exhaustive treatment on the use of optical remote sensing techniques applied for analyzing the glacier characteristics of Himalayan region. The relation between meteorology and glacier mass balance was studied in Chhota Shigri glacier catchment by Azam et al (2016), while a decadal scale snow and ice melt contribution was estimated for the same glacier catchment (Azam et al., 2019). Normalised Difference Snow Index (NDSI) has been used to extensively to map the extent of snow cover in various parts of the world in including the Himalayas (Immerzeel et al., 2009; Gurung et al., 2011). Moderate Resolution Imaging Spectroradiometer (MODIS) snow cover products have been used not only for snow studies, but also in Accumulation Area Ratio (AAR) delineation. Specific mass balance of glaciers has also been arrived at using the AAR technique that has been reworked over the years (Kulkarni, 1992; Tawde et al, 2016; Tak and Keshari, 2020). With the advancement in remote sensing and modeling capabilities coupled with longer in situ records available at select high altitude locations, we can now have the opportunity for better estimates of snow and glacier contributions to flows of Himalayan rivers.

1.2 Problem Definition

Water Resources in the Western Himalayan Region are dominantly sourced from snow and glacier reserves that get replenished at annual, decadal and even longer time scales. However, a lack of understanding of the multiple processes driving cryospheric response in the region limits our ability to anticipate consequent changes and their impacts (Wani et al, 2021). River Chenab originating in the highly glaciated and snow covered slopes of Pir Panjal Range in Lahaul and Spiti District of Himachal Pradesh is a source of water for parts of Himachal Pradesh and Jammu & Kashmir. Moreover, this river and its tributaries, with a huge hydropower potential is being tapped through several nationally important run-of-the river Hydro-Electric Projects in operation and various stages of planning and execution. Hence, it is critical to have reliable periodic assessments of the water resources locked up in snow and glaciers of the Upper Chenab Basin so that the water resource as well as the meltwater discharge component can be estimated. Several estimates at regional scale as well as catchment scale are reported in literature. But, there is a demand for current estimates of these cryospheric components that capture the first two decades of the 21st Century that reportedly are by far the warmest globally as well as regionally.

1.3 Objectives

The present study aims to assess the changes in snow and glacier resources in the Upper Chenab River Basin, Himachal Pradesh. The study will also investigate the climate-cryosphere linkages in this basin in view of the dependence of water availability on cryospheric resources. Keeping this in view, the following objectives were set for the study:

a) Investigation of snow cover changes and cryosphere-climate linkages in Upper Chenab River Basin (UCRB)

b) Estimation of specific glacier mass balance in Upper Chenab River Basin

1.4 Chapterization

The report is structured and organized into five chapters as follows:

Chapter-1 presents an overview of the study, problem statement and specifies the major objectives. It also summaries the organization of the report.

Chapter-2 provides the description of study area i.e., Upper Chenab River basin as well as the selected representative glacier, Chhota Shigri, in brief.

Chapter-3 presents the data sets used along with the methodology followed for analysis of snow cover extent variability across space and time. It also discusses the climate change over the study period, which has direct implications on changing cryospheric response of the basin.

Chapter-4 presents the estimation of specific glacier mass balance in Upper Chenab River Basin, with special reference to Chhota Shigri Glacier, a representative glacier in UIB and WHR.

Chapter-5 summarizes the report in brief and presents the key conclusion drawn from the study. It also presents the limitation of the present work and scope for future study.

CHAPTER 2

STUDY AREA

2.1 Upper Chenab River Basin

Upper Chenab River Basin (~3,728 km2) located in the Lahaul-Spiti District of Himachal Pradesh (76.87° E to 77.80° E and 32.08° N to 32.99° N), is composed of Chandra (~2,440 km^2) and Bhaga (~1,288 km^2) sub-basins, which join together near Tandi, Himachal Pradesh to form the mighty Chenab. Also called Chandra-Bhaga, it is one of the most glaciated basins in Western Himalayan Region, with estimates of snow and glacier contributions estimated between 50-80%. This basin is also interesting from the point of view of climatology as it falls under the monsoon-arid transition zone. Upper Chenab River Basin (UCRB) is alternately influenced by Mid-latitude Westerlies and Indian Summer Monsoon, although most of the accumulation happens in winter months.

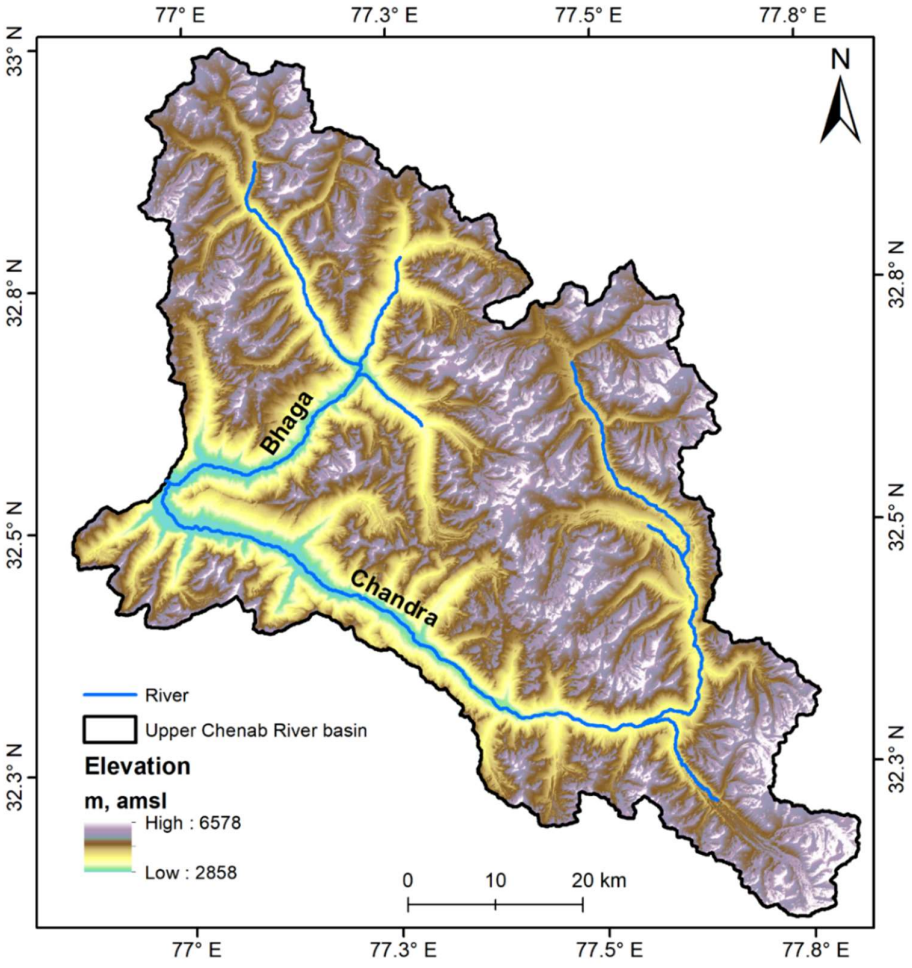

Figure 1: Location of study area (SRTM DEM), Upper Chenab River Basin

There is also a gradual increase in aridity as we go from SE to NW. Upper Chenab has one of the longest in situ glacier mass balance series in HKH region as well as year-round meteorological observations at glacier elevations, viz. Chhota Shigri Glacier, Chandra sub-basin. Apart from this, it also has long-term meteorological observations at a few locations both in the Chandra (eg. Koksar) and Bhaga (e.g. Patseo) sub-basins. Moreover, the basin is highly important from the point of hydropower generation, and several run-of-the-river hydroelectric projects (HEPs) depend on snow and glacier melt contributions that peak in summer months for their power generation.

2.2 Chhota Shigri Glacier

Chhota Shigri Glacier (CSG) is a valley glacier located in the Lahaul-Spiti region of Himachal Pradesh, India, on the northern slopes of the Pir Panjal Range of the western Himalaya (Fig 1). The glacier lies between approximately 32.28°N, 77.58°E, with an elevation range from about 4,100 m at the snout (terminus) in recent years up to ~5,830 m at the highest peaks feeding the accumulation zone (Wagnon et al., 2007; Vincent et al., 2013). Chhota Shigri is about 9 km long and has an area of roughly 15.5 km² as of 2020 (Azam et al., 2018; Srivastava et al., 2022). The glacier's accumulation zone is bounded by steep ridges including Devachan Peak (6,250 m) to the east. Several tributary ice streams contribute to Chhota Shigri; notably, an eastern tributary joins the main trunk, and until 2012 a western tributary was connected but has since detached due to glacier wastage (Srivastava et al., 2022). The lower 2–3 km of the glacier (below ~4,500 m) is debris-covered, with rock debris insulating parts of the ablation zone. Approximately 12% of the glacier's surface area is debris-covered, including a prominent medial moraine and lateral moraines along the tongue (Azam et al., 2016; Azam et al., 2024). Debris thickness varies from just a few centimetres in places to several meters with large boulders near the terminus. Above the debris-covered zone, the glacier's surface consists of clean ice and seasonal snow in the accumulation areas, which have aspects ranging northward and northeast.

Hydrologically, Chhota Shigri Glacier is part of the Chandra River basin. Meltwater from the glacier flows into a proglacial stream that joins the Chandra River, which later becomes the Chenab River downstream. Because of this, the glacier is an important source of summer meltwater for the region. Climatic setting: The glacier lies in a transitional climatic zone influenced by both the Indian Summer Monsoon (ISM) and the mid-latitude westerlies. Typically, the summer monsoon (July–September) brings precipitation to the area, while the winter westerlies (December–April) contribute snow at higher elevations. As a result, Chhota Shigri is often described as a "maritime" glacier in terms of precipitation regime, receiving substantial snowfall in both summer and winter. The annual mass balance of the glacier is sensitive to variations in both summer melt (governed by temperature and monsoon conditions) and winter accumulation (snowfall from westerlies) (Wagnon et al., 2007). Observational records indicate that the equilibrium line altitude (ELA) on Chhota Shigri typically ranges around 5,000–5,200 m in recent years, but can vary with annual climate conditions (Azam et al., 2018).

Chhota Shigri Glacier has been studied extensively. A four-year field study (Wagnon et al., 2007) established it as a benchmark glacier with an average annual mass balance around –0.6 m w.e. per year in the early 2000s, and subsequent annual measurements by Indian and French teams have documented interannual fluctuations and trends. These field data provide a valuable baseline: for instance, Vincent et al. (2013) noted that CSG had near-balanced mass budgets in the 1990s, but then sustained mass loss after 2000. The long-term monitoring makes CSG one of the best-recorded glaciers in the Himalaya, and its data have been used to validate remote sensing methods (Pandey & Venkataraman, 2013) and improve glacier models (Azam et al., 2016; Engelhardt et al., 2017). The significance of Chhota Shigri also lies in its representativeness – it has been classified as a "tier 2" reference glacier for the region (Paul et al., 2007), meaning it is thought to be broadly indicative of glacier behavior in the northwestern Himalaya. Thus, findings from Chhota Shigri often inform regional assessments of climate change impacts on water resources. At the same time, local topographic factors (such as its debris cover and valley geometry) mean that detailed, glacier-specific studies are necessary to fully understand its dynamics.

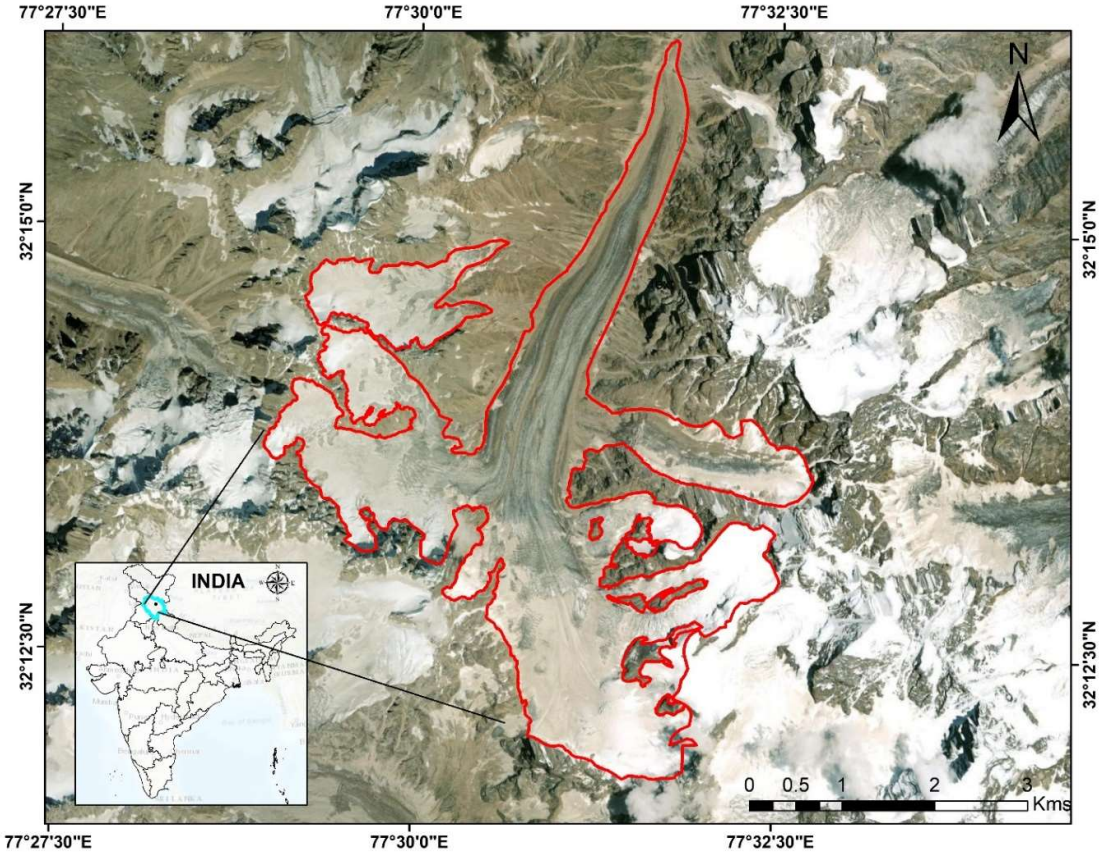

Fig. 1 Study Area Map of Chhota Shigri Glacier

CHAPTER 3

INVESTIGATION OF SNOW COVER CHANGES AND CRYOSPHERE-CLIMATE LINKAGES IN UPPER CHENAB RIVER BASIN

3.1 Overview

A significant portion of the Himalayan landscape is dominated by glaciers and transient snow cover. These cryospheric elements play a crucial role in influencing water resources in mountainous regions. However, their specific impacts in the Himalayan region remain poorly understood, primarily due to insufficient observational data. Snow cover is a critical land surface parameter in the global water and energy cycles, as it regulates radiation feedback on both global and regional scales and serves as a reservoir for freshwater within the hydrological cycle. At a regional level, snow cover is vital for local water availability, river discharge, and groundwater recharge, particularly in middle and high latitudes (Jain et al., 2008). In the North Western Himalayas (NWH), extensive areas receive precipitation in the form of snow due to low winter temperatures and high-altitude terrain. The meltwater from snow and glaciers significantly contributes to the flow of major rivers in the NWH. Hydrological models often incorporate snow-covered area (SCA) data alongside hydro-meteorological variables to simulate snowmelt runoff (Aggarwal et al., 2013). However, traditional methods of mapping and monitoring seasonal snow cover face considerable challenges, including sparse snow gauges, inaccessible terrain during winter, rugged topography, and the remoteness of these regions. Satellite-based remote sensing has emerged as a powerful tool for mapping and monitoring snow cover, glacier extents, and high-altitude lakes in these areas, offering high temporal and spatial resolution (Aggarwal et al., 2013).

The Terra (EOS AM) and Aqua (EOS PM) satellites, equipped with the Moderate-Resolution Imaging Spectroradiometer (MODIS) sensor, have provided daily, 8-day, and 16-day SCA products since 2000. Among these, the MOD10A2 and MYD10A2 products, which offer 500-meter resolution 8-day maximum snow cover data (Dorothy et al., 2001), have been extensively utilized for snow cover estimation (Snehmani et al., 2016; Shukla et al., 2018). These products are generated using a snow mapping algorithm that relies primarily on the Normalized Difference Snow Index (NDSI) and additional criteria tests (Hall et al., 1995).

In recent decades, the Himalayan region has experienced accelerated glacier melt due to global warming, a trend observed over the past 40 years (Maurer et al., 2019). Rising temperatures are expected to further impact snow cover extent, subsequently affecting the discharge of snow-fed rivers. Reanalysis products such as ERA5-Land, which provide long-term climatological data, can be instrumental in exploring the linkages between climate and cryospheric changes. For instance, Dharpure et al. (2020) utilized ERA5-Land reanalysis data to assess the effects of climate change on snow cover dynamics in the Chenab River basin.

There is a pressing need for comprehensive investigations into snow cover extent in relation to regional climatology to enhance the existing knowledge base. Current studies often

focus on large-scale analyses, encompassing either the entire northwestern Himalayas or the complete Himalayan range, thereby overlooking regional nuances. Additionally, the availability of satellite imagery since 2000, coupled with finer-scale reanalysis products, presents an opportunity to derive valuable insights into the impacts of climate change on snow cover dynamics. Such efforts are essential for understanding and addressing the challenges posed by changing climatic conditions in the Himalayan region. Considering the above discussion in view the following sub-objectives were formulated:

1) To analyze the spatial distribution of snow cover extent in Chandrabhaga River basin with respect to elevation, slope, and aspect
2) To analyze the seasonal variability in snow cover extent in Chandrabhaga River basin
3) To investigate the impact of climate change

3.2 Data Used

In this study, remote sensing data derived from MODIS imagery were utilized to analyze the spatial and temporal variability of snow cover extent, while ERA5-Land reanalysis data were employed to examine the long-term climatology of the basin. For topographic classification of the basin the ALOS Global Digital Surface Model (DSM) was utilized. A brief description of these datasets is provided below.

3.2.1 MODIS remote sensing data

MOD10A2 is a snow cover dataset derived from the Moderate Resolution Imaging Spectroradiometer (MODIS) onboard the Terra satellite. This dataset provides the maximum snow cover extent observed over an eight-day period at a spatial resolution of 500 meters. The eight-day compositing period aligns with the ground track repeat cycle of the Terra and Aqua satellite platforms, ensuring consistent temporal coverage. Within each composite period, snow cover is represented in two ways: as the maximum snow extent observed on any single day and as a chronological sequence of daily observations. The eight-day periods are calculated starting from the first day of the year and may extend into the following year. While the product is designed to include up to eight days of input data, the actual number of days may vary due to factors such as cloud cover or data acquisition issues. This dataset has been widely used for monitoring snow cover dynamics, hydrological modeling, and climate studies due to its high temporal and spatial resolution.

3.2.2 ALOS Global Digital Surface Model

The ALOS Global Digital Surface Model (AW3D30) is a high-resolution global dataset derived from imagery captured by the Panchromatic Remote-sensing Instrument for Stereo Mapping (PRISM) onboard the Advanced Land Observing Satellite (ALOS), operational from 2006 to 2011. Developed by the Japan Aerospace Exploration Agency (JAXA), the dataset provides a horizontal resolution of approximately 30 meters (1 arcsecond) and is freely available for use. It is based on the "World 3D Topographic Data," a 5-meter mesh DSM, and is recognized as one of the most precise global elevation datasets currently available. The

AW3D30 dataset is widely regarded for its exceptional elevation accuracy and is valuable for applications in scientific research, education, and private-sector geospatial services. Its high precision and global coverage make it a critical resource for topographic analysis, environmental studies, and land surface modeling.

3.2.3 ERA5-Land data

ERA5-Land is a high-resolution (0.1° x 0.1°) reanalysis dataset that offers a consistent and comprehensive view of land surface variables over multiple decades. Produced by replaying the land component of the ECMWF ERA5 climate reanalysis, it integrates model data with global observations using physical laws to generate a globally complete and temporally consistent dataset. The dataset spans several decades, enabling the analysis of long-term climatic trends and historical land surface conditions.The atmospheric forcing for ERA5-Land is derived from ERA5 atmospheric variables, including air temperature, humidity, and pressure, which are corrected for altitude differences between the forcing grid and the higher-resolution ERA5-Land grid using a 'lapse rate correction.' While observations are not directly assimilated into ERA5-Land, they indirectly influence the dataset through the atmospheric forcing, ensuring a realistic representation of land surface processes. The dataset's high temporal and spatial resolution, combined with its extensive temporal coverage and fixed grid structure, makes it a powerful tool for researchers, decision-makers, and businesses seeking accurate and reliable information on land surface states and dynamics. For this study, three ERA5-land datasets (Table 3.1) were obtained for the period spanning 1950-2021.

Table 3.1 Description of ERA5-Land hourly data used

S. No.	Data	Description
1	2m temperature (K)	Temperature of air at 2m above the surface of land, sea or in-land waters.
2	Snowfall (m.w.e.)	Accumulated total snow that has fallen to the Earth's surface. It consists of snow due to the large-scale atmospheric flow (horizontal scales greater than around a few hundred metres) and convection where smaller scale areas (around 5km to a few hundred kilometres) of warm air rise. If snow has melted during the period over which this variable was accumulated, then it will be higher than the snow depth. This variable is the total amount of water accumulated from the beginning of the forecast time to the end of the forecast step.
2	Total precipitation (m)	Accumulated liquid and frozen water, including rain and snow, that falls to the Earth's surface. It is the sum of large-scale precipitation (that precipitation which is generated by large-scale weather patterns, such as troughs and cold fronts) and convective precipitation (generated by convection which occurs when air at lower levels in the atmosphere is warmer and less dense than the air above, so it rises). Precipitation

		variables do not include fog, dew or the precipitation that evaporates in the atmosphere before it lands at the surface of the Earth. This variable is accumulated from the beginning of the forecast time to the end of the forecast step.

3.3 Methodology

3.3.1 Snow cover analysis

The methodology employed in this study to analyze the snow cover dynamics of the Chandrabhanga River basin is both comprehensive and systematic, leveraging advanced remote sensing and geospatial techniques to ensure robust and reliable results. A total of 939 MODIS images from the TERRA satellite, specifically the MOD10A2 product—an eight-day composite land surface reflectance dataset—were acquired for the period spanning 2000 to 2020. This product is particularly valuable as it provides the maximum extent of snow cover observed over an eight-day period at a spatial resolution of 500 meters, capturing the days on which snow was present within this timeframe. The maximum snow extent is defined as areas where snow was detected on at least one day during the eight-day interval, offering a detailed temporal perspective on snow cover variability. To facilitate a nuanced analysis of snow cover distribution, the Chandrabhanga River basin was stratified into distinct zones based on elevation, slope, and aspect, which are critical topographic factors influencing snow accumulation and melt processes. Prior to this stratification, the ALOS Global Digital Surface Model (DSM), with a high spatial resolution of 30 meters, was utilized to generate detailed elevation, slope, and aspect maps of the study area. These maps served as the foundational datasets for delineating the basin into 03 elevation bands (Fig. 3.1), six slope bands (Fig. 3.2) and eight aspect bands (Fig. 3.3.) as detailed in Table 3.2.

Table 3.2 Elevation, slope and aspects band classification

Elevation bands	Slope bands		Aspect bands	
a) 2800–4000 m, a.m.s.l.	a) 0–10°	d) 30–40°	a) North	e) South
b) 4000–5200 m, a.m.s.l.	b) 10–20°	e) 40–50°	b) North-East,	f) South-West,
c) >5200 m, a.m.s.l.	c) 20–30°	f) >50°	c) East	g) West, and
			d) South-East	h) North-West

3.3.2 Climatological analysis

ERA5-Land data, renowned for its high temporal and spatial consistency, ensures robust insights into the interplay between climatic variables and snow cover dynamics, thereby enhancing the scientific understanding of cryospheric responses to global warming. To investigate the influence of global warming, driven by climate change, on snow cover dynamics, ERA5-Land hourly datasets for total precipitation and air temperature were acquired for the length of 72-year from 1950 to 2021. These datasets, available at a spatial resolution of 9 km × 9 km, provide a seamless and comprehensive spatiotemporal record for analysis.

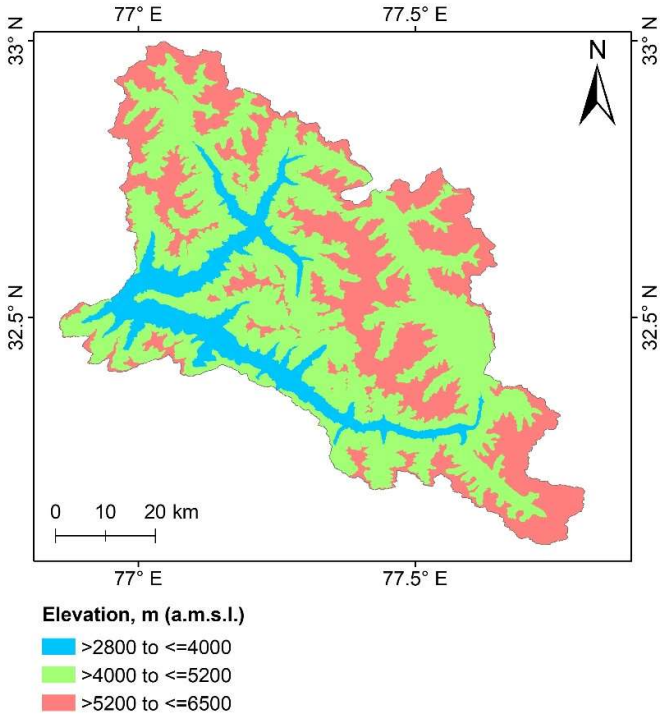

Fig. 3.1 Categorized elevation bands in Chandrabhaga River basin

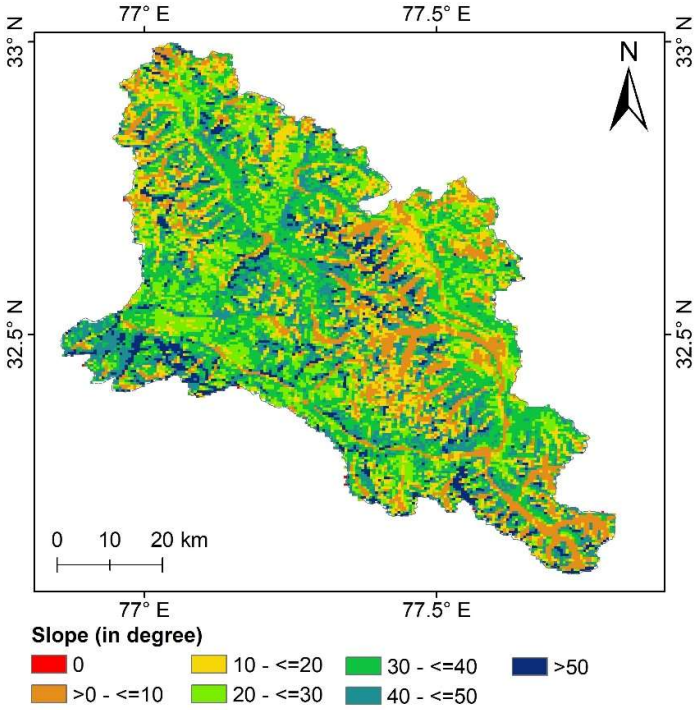

Fig. 3.2 Categorized slope bands in Chandrabhaga River basin

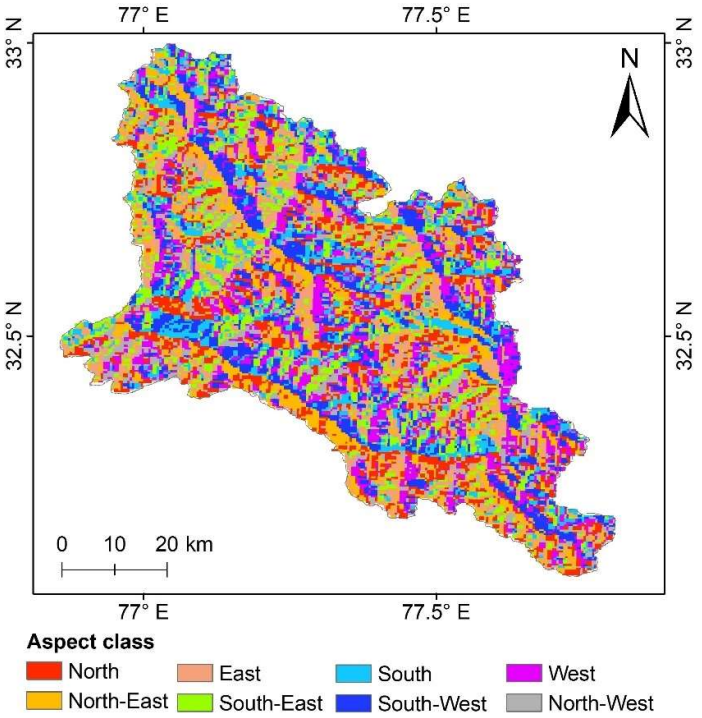

Fig. 3.3 Categorized aspect bands in Chandrabhaga River basin

The ERA5-Land reanalysis data were utilized to derive regional mean monthly climatology, specifically focusing on mean monthly precipitation and mean monthly temperature. These climatological signatures are presented in Fig. 3.4 and Fig. 3.5, respectively, offering a detailed depiction of long-term climatic signals in the study region.

3.3.3. Statistical analysis

To extract meaningful insights from climatological data, the time series were systematically analyzed for trends. The Modified Mann-Kendall test, a robust non-parametric method for trend detection, was employed to assess trends in snowfall and temperature. These analyses were conducted across multiple 30-year climatic windows—1951–1980, 1961–1990, 1971–2000, 1981–2010, and 1991–2020—along with an evaluation of the long-term trend spanning the entire period of record (1950–2020). The magnitude of statistically significant trends was quantified using Thiel-Sen's slope estimator. All trend analyses were performed at a 5% significance level. A comprehensive description of the Modified Mann-Kendall test and Thiel-Sen's slope estimation methodology is provided in Bisht et al. (2018). Furthermore, the anomaly in the snowfall and temperature were studied with respect to the reference period of 1961-1990 to understand the shift in these climatological variables. Furthermore, the anomalies in the Positive Degree Days (PDD) across the basin were also studied to understand how the PDDs have changed over the period.

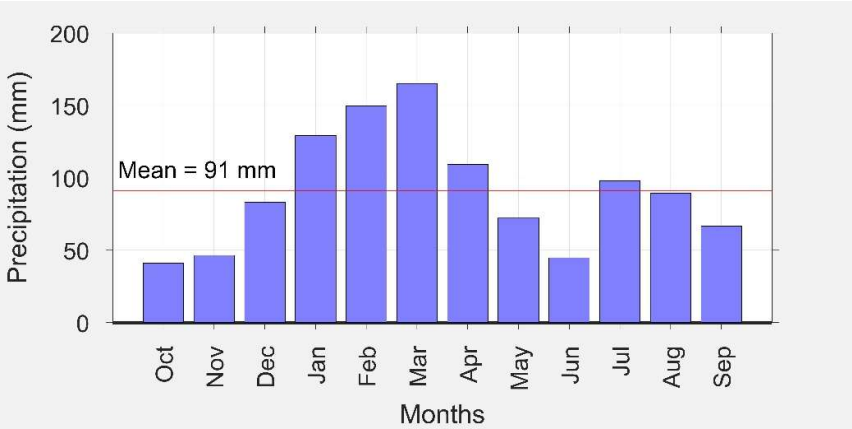

Fig. 3.4 Mean monthly Precipitation pattern of the Chandrabhaga River basin as revealed by ERA5 monthly data during 1950-2021

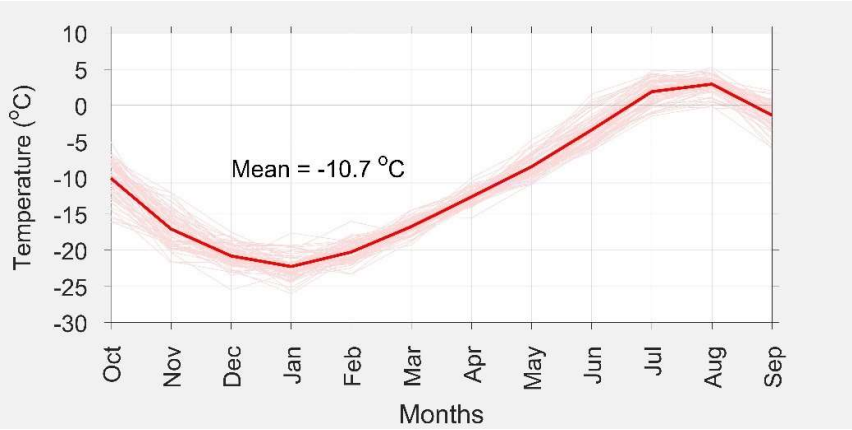

Fig. 3.5 Mean monthly temperature variation of the Chandrabhaga River basin as revealed by ERA5 monthly data during 1950-2021

3.4 Result and Discussion

3.4.1 Spatial distribution of snow cover extent in Chandrabhaga River basin

The multi-criteria stratification of the basin based on altitude, slope and aspects allow for a granular examination of snow cover dynamics across diverse topographic conditions. The variation in snow cover extent was quantified with respect to maximum, minimum, and average snow cover values over the 20-year study period, with results systematically analysed for each elevation band, slope band, and aspect. This approach not only enhances the understanding of spatial and temporal snow cover patterns but also provides critical insights into the interplay between topography and cryospheric processes, which is essential for hydrological modeling, climate change impact assessments, and water resource management in high-altitude regions.

(a) Snow cover extent vs elevation

The variation in annual snow cover extent with respect to elevation in the Chandrabhaga River Basin during 2000–2020 is summarized in Table 3.3. The analysis considers three elevation zones: Zone 1 (2800–4000 m), Zone 2 (4000–5200 m), and Zone 3 (>5200 m), along with the entire basin area above 2800 m.

The total area above 2800 m in the basin spans 4084 km², with an average annual snow cover percentage of 83.6%. Among the elevation zones, Zone 1 (2800–4000 m), which covers an area of 482 km², exhibits the lowest snow cover extent, with an annual average of 55.3%. Zone 2 (4000–5200 m), encompassing 2256 km², experiences higher snow coverage, with an average annual snow cover percentage of 82.3%. The highest elevation range, Zone 3 (>5200 m), covering 1346 km², has the most persistent snow cover, with an annual average snow cover percentage of 96.4%.

Table 3.3 Variation in annual snow cover extent w.r.t. elevation in Chandrabhaga River basin during 2000-2020

Elevation zone	Elevation band (m, amsl)	Areal extent (km^2)	Pixel count	Percentage annual areal snow cover		
				Max	Min	Average
Entire	>2800	4084	19024	100	47.9	83.6
Zone 1	2800-4000	482	2246	100	0.90	55.3
Zone 2	4000-5200	2256	10509	100	34.2	82.3
Zone 3	>5200	1346	6269	100	83.2	96.4

These findings highlight a strong correlation between elevation and snow cover extent, with higher elevations experiencing more persistent and extensive snow coverage. This variation is crucial for understanding snow accumulation and melt patterns, which influence hydrological processes in the Chandrabhaga River Basin.

(b) Snow cover extent vs slope

The analysis of annual snow cover extent in the Chandrabhaga River basin during 2000–2020 reveals a distinct relationship between snow cover distribution and slope variations. Table 3.4 categorizes the basin into six slope zones, ranging from nearly flat terrain (Zone 1: 0–10°) to steep slopes exceeding 50° (Zone 6), along with a separate category (Zone 0) for areas where slope data were not applicable.

Table 3.4 Variation in annual snow cover extent w.r.t. slope in Chandrabhaga River basin during 2000-2020

Slope class	Slope range (Degree)	Areal extent (km^2)	Pixel count	Percentage annual areal snow cover		
				Max	Min	Average
Zone 0	NA	2	7	100	69.3	96.9
Zone 1	0-10	597	2780	100	67.6	89.0
Zone 2	10-20	694	3233	100	59.8	88.6
Zone 3	20-30	744	3468	100	32.8	78.5
Zone 4	30-40	1161	5409	100	32.9	78.7

Zone 5	40-50	659	3069	100	53.5	86.5
Zone 6	> 50	255	1187	100	61.6	87.6

Zone 0, showing the limited areal extent of 2 km², exhibited the highest average annual snow cover percentage (96.9%), indicating persistent snow accumulation in these areas. In Zone 1 (0–10° slope), covering 597 km², the annual snow cover percentage remained high, averaging 89.0%. A similar trend was observed in Zone 2 (10–20°), where an areal extent of 694 km² corresponded to an 88.6% annual snow cover. As the slope increased beyond 20°, a notable decline in snow cover percentage was observed. Zone 3 (20–30°) and Zone 4 (30–40°) had relatively large areal extents of 744 km² and 1161 km², respectively, yet their snow cover percentages dropped to 78.5% and 78.7%, indicating increased snowmelt and redistribution on steeper slopes. Conversely, Zone 5 (40–50°) showed an increase in snow cover percentage (86.5%), despite having an areal extent of 659 km². This suggests localized variations in snow retention, possibly due to topographic shading or aspect-related influences. Similarly, Zone 6 (>50° slope) exhibited a comparable snow cover percentage of 87.6%, though it had the smallest areal extent of 255 km².

From the finding it can be said that while gentler slopes tend to retain more snow cover, variations exist across steeper terrain due to complex interactions between topography, solar radiation, and wind redistribution. The results highlight the significance of slope as a controlling factor in snow cover distribution within the Chandrabhaga River basin.

(c) Snow cover extent vs aspect

The analysis of annual snow cover extent across different slope aspects, shown in Table 3.5, in the Chandrabhaga River Basin from 2000 to 2020 reveals significant variation in snow persistence. North-facing slopes (Zone 1) exhibit the highest average percentage of annual snow cover (86.9%). Similarly, the North-West (Zone 8) and North-East (Zone 2) aspects also show high snow retention, with average annual snow cover percentages of 86.5% and 84.7%, respectively.

Table 3.5 Variation in annual snow cover extent w.r.t. aspect in Chandrabhaga River basin during 2000-2020

Slope class	Aspect range	Areal extent (km^2)	Pixel count	Percentage annual areal snow cover		
				Max	Min	Average
Zone 1	North	539	2510	100	55.4	86.9
Zone 2	North-East	526	2450	100	48.2	83.7
Zone 3	East	549	2559	100	50.5	85.8
Zone 4	South-East	497	2313	100	46.4	83.5
Zone 5	South	454	2114	100	43.8	80.6
Zone 6	South-West	562	2620	100	36.3	77.6
Zone 7	West	537	2503	100	45.5	83.7
Zone 8	North-West	420	1955	100	53.1	86.5

In contrast, south-facing slopes (Zone 5) experience lower snow retention, with an average annual snow cover of 80.6%. The South-West aspect (Zone 6) records the lowest

percentage of annual snow cover at 77.6%, indicating a relatively higher rate of snowmelt. East-facing (Zone 3) and West-facing (Zone 7) slopes exhibit intermediate snow cover values of 85.8% and 83.7%, respectively, while the South-East (Zone 4) aspect records 83.5% coverage. The minimum snow cover extent provides critical insights into snow retention patterns, revealing significant variability across different aspects. South-facing aspects exhibit the highest snow loss, as evidenced by the minimum snow cover extent in the South-West (Zone 6), South (Zone 5), and South-East (Zone 4) aspects, where snow cover drops to 36.3%, 43.8%, and 46.4%, respectively. In contrast, North-facing aspects demonstrate greater snow retention, with minimum snow cover remaining significantly higher at 55.4% and 53.1% for the North (Zone 1) and North-West (Zone 8) aspects, respectively.

The contrast in snow retention highlights the influence of aspect on snowmelt dynamics, with South-facing slopes experiencing more pronounced snow loss due to greater exposure to solar radiation, while North-facing slopes retain snow more effectively. The findings underscore the importance of aspect-based analysis in understanding snow dynamics, which has implications for hydrological modeling and water resource management in the region.

3.4.2 Seasonal variability in snow cover extent in Chandrabhaga River basin

The snow cover variability was also examined on monthly basis across the basin during 2000-2020. For this a total of 931 MODIS images were analysed. Monthwise variability of snow cover is presented in Fig. 3.6. It is to be noted that, the monthwise snow cover variability was presented for the days for which cloud cover is found to be less than 15 %. Cloud cover extent for respective snow cover variabilities presented in Fig. 3.6 is illustrated in Fig. 3.7. For a cloud cover of 15% or more over the basin the snow cover analysis was excluded to avoid potential errors due to data gap.

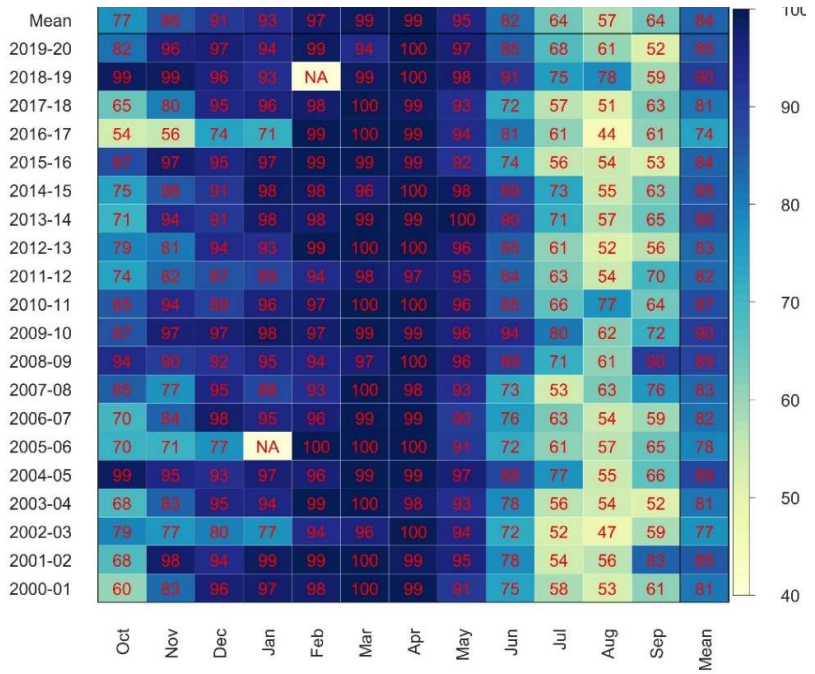

Fig. 3.6 Variation in month-wise average snow cover extent (in % of total basin area) during 2000-2020.

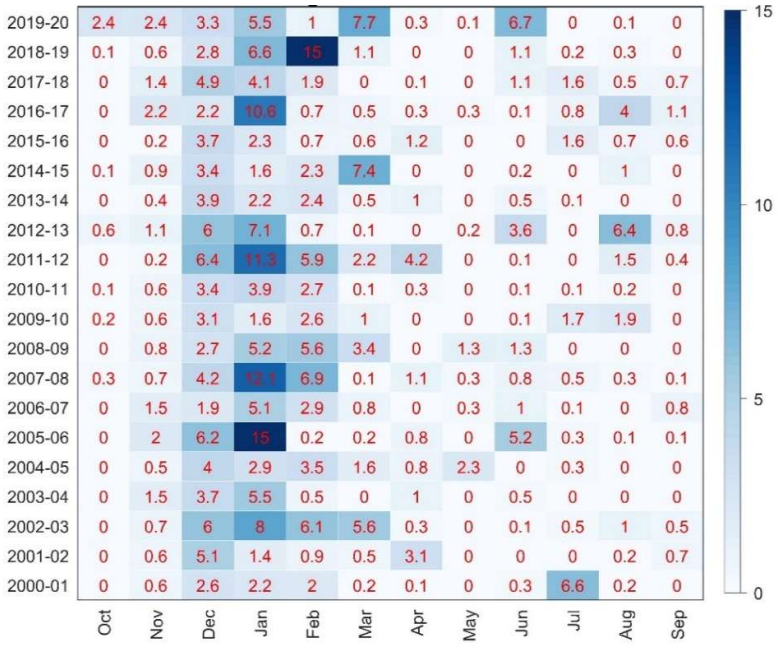

Fig. 3.7 Average cloud cover extent in the analysis of monthwise variability in snow cover extent during 2000-2020

The month-wise variation in average snow cover extent in the Chandrabhaga River Basin from 2000 to 2020 highlights distinct seasonal patterns. The analysis shows that snow cover varies significantly across months, with peak coverage occurring in late winter and early spring, followed by a gradual decline during summer and monsoon months.

During the colder months of December to March, the basin experiences extensive snow cover, averaging above 90% of the total area. Maximum coverage is observed in March (99%), followed by February (97%) and January (93%), indicating that winter months contribute significantly to snow accumulation. Snow cover remains high in April (99%) and May (95%), suggesting a slow onset of snowmelt. From June onward, snow cover declines rapidly due to rising temperatures. June records an average snow extent of 82%, which further decreases to 64% in July. The lowest snow cover is observed in August (57%), corresponding to peak summer and monsoon conditions, before a slight recovery in September (64%) and October (77%) as fresh snowfall begins.

Interannual variations are evident, with some years experiencing significantly higher snow cover due to variations in winter precipitation. Notably, the hydrological years 2004–2005, 2009–2010, and 2018–2019 exhibit particularly high snow coverage throughout most months, with average annual snow cover reaching close to 90%. In contrast, 2016–2017 recorded the lowest average snow extent (74%), reflecting potential anomalies in snowfall patterns.

The analysis underscores the seasonal and interannual variability in snow cover, which has critical implications for water availability, glacier dynamics, and hydrological processes in the basin. The findings are particularly relevant for understanding long-term climate trends, snowmelt-driven runoff, and water resource management in the region.

3.4.3 Impact of climate change

The climatological data were analyzed at multiple temporal scales to assess both long-term and short-term trends, providing a comprehensive understanding of climatic variability and its impacts on snow cover dynamics. This included an evaluation of the long-term series spanning 1950–2020, as well as shorter 30-year climatic windows for the periods 1951–1980, 1961–1990, 1971–2000, 1981–2010, and 1991–2020. Additionally, a 5-year moving window analysis was conducted to examine changes in the rolling mean over the study period. These analyses were performed at both grid-wise and regional scales to capture basin-specific responses as well as broader regional distribution patterns. Special emphasis was placed on the summer season (May–October) to investigate changes in summer temperatures and snowfall over time, alongside an assessment of anomalies in positive degree days, which are critical drivers of snowmelt. The frequency of these anomalies was evaluated relative to the baseline period of 1961–1990. Furthermore, regional trends in snowfall were analyzed to understand how snowfall patterns have changed on both annual and seasonal scales, with the summer (May–October) and winter (November–April) seasons examined separately. Regional snowfall anomalies were also computed to quantify shifts in snowfall patterns relative to the baseline period, offering insights into the evolving climatic influences on snow cover dynamics. The findings of these analysis of temperature and snowfall time series are discussed in subsequent sections.

3.4.3.1 Snowfall

Analysis of long-term ERA5-Land data (1951–2020) reveals that the Chandrabhaga River basin primarily receives precipitation in the form of snowfall (Fig. 3.8). However, during the active months of the Indian Summer Monsoon (June–September), liquid precipitation (rainfall) exceeds solid precipitation (snowfall).

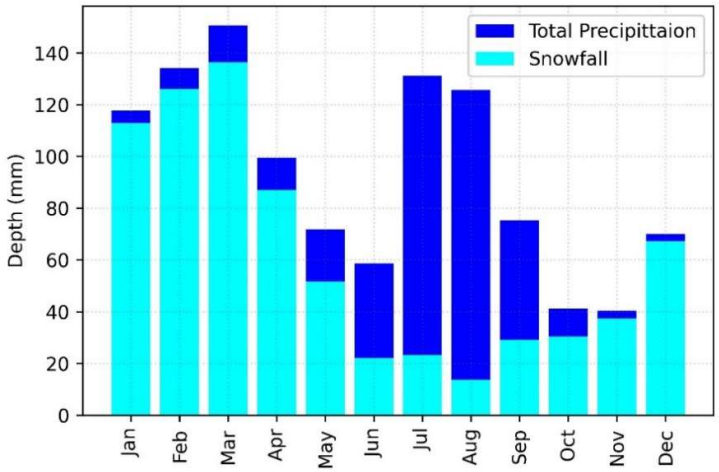

Fig. 3.8 Total precipitation vs Snowfall in Chandrabhaga River basin (averaged over 1951-2020)

The snowfall observed from November to May is largely attributed to western disturbances, which transport significant moisture to the region. Over time, global warming has altered regional precipitation patterns, affecting both Himalayan and the broader global climate system. Given its hydrological significance, the Chandrabhaga River basin plays a crucial role in sustaining downstream populations in the Jammu and Kashmir region, making its precipitation dynamics of critical importance. Therefore, it is also important to understand how the precipitation regime has changed over the period.

In the snow-capped regions of the high mountains in the Himalayas, winter precipitation plays a crucial role, as the majority of moisture is received in the form of snow. This accumulated snow gradually melts during the summer, contributing to streamflow through snowmelt and glacier melt. Therefore, an analysis was conducted to examine the seasonal behavior of precipitation, specifically summer (May–October) and winter (November–April) precipitation, along with annual precipitation patterns, to assess anomalies. Given that snowfall constitutes a significant portion of the total precipitation, its changing pattern was evaluated in terms of anomalies—deviations from the baseline period (1961–1990)—and directional trends. Additionally, as rising temperatures directly impact snowfall, leading to its reduction and altering its pattern, liquid precipitation was excluded from subsequent analyses.

To assess the variation in snowfall patterns over the region, snowfall anomalies were calculated relative to the baseline period (1961–1990), a widely adopted reference period in climatological studies. The anomaly was computed for annual, summer, and winter snowfall to understand deviations from the historical norm, as illustrated in Fig. 3.9. The analysis revealed a significant interannual variability in snowfall anomalies.

Annual snowfall anomalies exhibit a complex pattern, with the highest positive deviation occurring in 1957 (396 mm w.e.), suggesting an exceptionally high snowfall year, while severe negative anomalies are recorded in 2001 (-302 mm w.e.) and 2016 (-316 mm w.e.), indicating significantly lower-than-average snowfall. Notably, the summer anomaly exhibits extreme positive deviations in years such as 1950 (147 mm w.e.), 1955 (260 mm w.e.), 1957 (217 mm w.e.), and 1998 (152 mm w.e.), suggesting anomalously high summer snowfall during these years. Conversely, substantial negative anomalies are observed in 2016 (-107 mm w.e.), 2000 (-85 mm w.e.), and 1978 (-88 mm w.e.), indicating lower-than-average summer snowfall. The winter snowfall anomaly also demonstrates considerable fluctuations, with extreme negative values recorded in 1970 (-230 mm w.e.), 2000 (-250 mm w.e.), and 2017 (-273 mm w.e.), highlighting years of significantly reduced winter snowfall. In contrast, positive winter anomalies such as in 1972 (246 mm w.e.), 1991 (184 mm w.e.), and 1995 (175 mm w.e.) indicate periods of above-average winter snowfall.

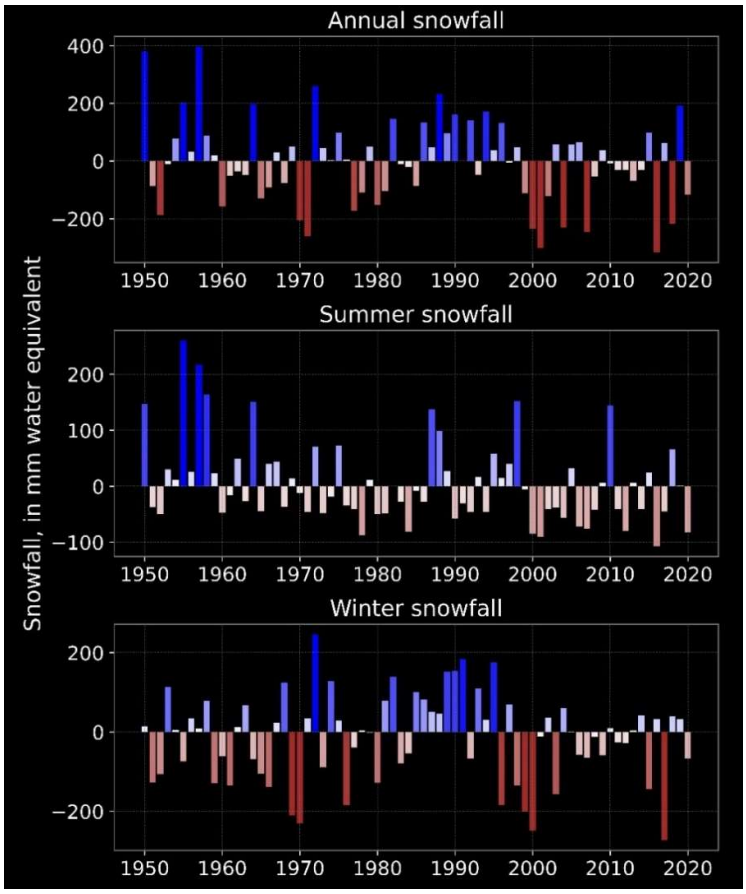

Fig. 3.9 Anomaly in regional snowfall w.r.t. baseline period: 1961-1990

The analysis revealed a clear declining trend in snowfall anomalies in recent decades, particularly post-2000, suggesting broader climatic changes impacting snowfall patterns in the region. Between 2000 and 2020, winter snowfall exhibited negative anomalies in 12 years, while summer and annual snowfall showed negative anomalies in 14 years. Notably, the magnitude of negative anomalies during this period was generally larger than that of positive anomalies, reinforcing the indication of a declining snowfall trend. This pronounced variability in snowfall anomalies is likely driven by regional climatic shifts, alterations in large-scale atmospheric circulation patterns, and evolving precipitation regimes, all of which contribute to the changing snowfall dynamics in the region.

(a) Snowfall trend

The spatial trend in snowfall was analyzed over a broader domain encompassing the Chandrabhaga River basin, rather than being restricted solely to the basin boundary. This approach was adopted to assess regional responses to climate change, recognizing that climate change is a large-scale phenomenon and is not confined within administrative or hydrological boundaries. The snowfall trends were evaluated using the Modified Mann-Kendall trend test, while the Thiel-Sen's slope estimator was employed to quantify the magnitude of trends. The analysis was conducted over the entire study period (1950–2020), spanning 71 years, as well as for five consecutive 30-year climatic windows: 1951–1980, 1961–1990, 1971–2000, 1981–2010, and 1991–2020. This approach enables a comprehensive understanding of both long-

term snowfall trends and their variability across different climatic periods, offering insights into how various atmospheric windows capture climate-induced changes in snowfall patterns.

For annual snowfall trends (Fig. 3.10), the analysis indicates an overall negative trend over the long-term period across the region. However, at a 5% significance level, the trend was not found to be statistically significant. A more detailed examination of the five climatic windows revealed noteworthy variations. The first climatic window (1951–1980) exhibited a negative trend, though not statistically significant across the region. This trend was subsequently reversed to a positive trend in the next two climatic windows (1961–1990 and 1971–2000), although no grid points within the basin boundary showed significant trends.

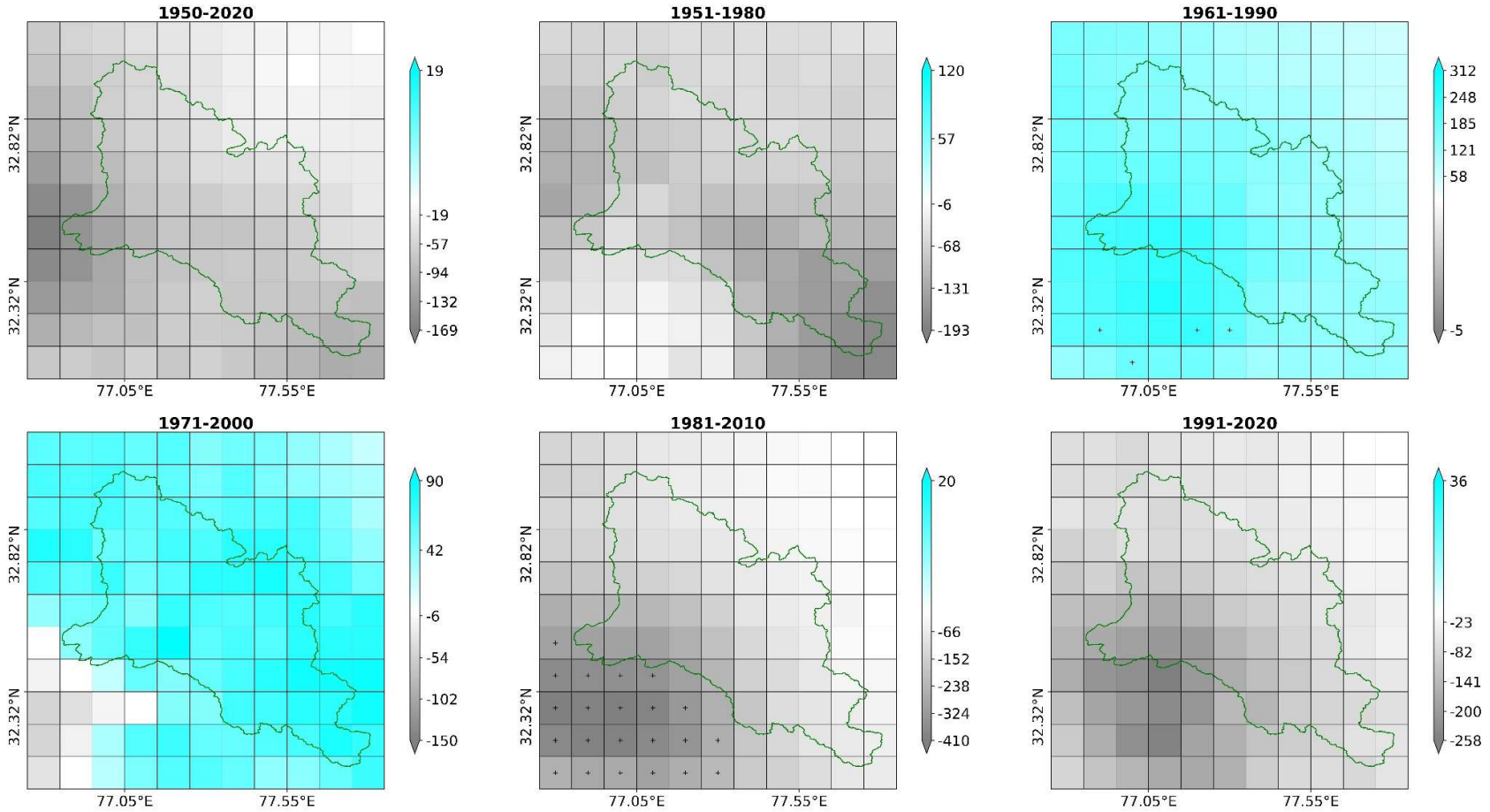

Fig. 3.10 Trend in annual snowfall, significant trends at 5% significance level are shown with dots (units in mm, w.e.)

In contrast, the trend shifted back to negative in the following two windows (1981–2010 and 1991–2020), with some regions in the southwestern part of the basin displaying a statistically significant strong negative trend during 1981–2010. However, in the most recent climatic window (1991–2020), while the declining trend persisted, no grid points exhibited statistically significant trends.

This variability in annual snowfall trends across different climatic windows highlights the complex nature of climate dynamics in the region. Notably, although the trends were not found to be statistically significant in most cases, the overall linear direction of the trend has remained negative over the last two climatic windows, covering the past 40 years since 1981. This persistent declining trend raises concerns about the long-term sustainability of snowfall in the region and its potential implications for hydrological and ecological systems.

Similarly, the snowfall trends were further analyzed for the summer season (May–October) to examine the temporal evolution of seasonal snowfall (Fig. 3.11). Unlike annual snowfall, where the long-term declining trends were not found to be statistically significant, summer snowfall exhibited a strong and statistically significant negative trend over the period 1951–2020 across the entire region. This negative trend persisted across different climatic windows, with all four climatic periods, except 1971–2000, displaying a pronounced decline in summer snowfall. The 1981–2010 climatic window showed some localized, albeit statistically insignificant, positive trends in the eastern part of the region. Interestingly, this same eastern region exhibited a statistically significant negative trend during 1951–1980, highlighting the spatial and temporal variability in snowfall patterns within the basin. The overall long-term negative trend in the summer snowfall, which is statistically significant, underscores an alarming decline in regional snowfall, likely attributable to climate change. This persistent reduction in summer snowfall has critical implications for water resource availability and hydrological processes in the region.

Since a significant portion of snowfall occurs during the winter season (November–April), a seasonal trend analysis of winter snowfall was conducted (Fig. 3.12). The results revealed mixed trends over the long-term period (1950–2020), with a distinct spatial division along the southeast-northwest axis. The eastern part, along the southeast-northwest axis, of the region exhibited a predominantly positive trend, whereas the western part, along the southeast-northwest axis, showed largely negative trends. However, none of these trends were found to be statistically significant. Mixed trends were also found for the climatic window of 1951-1980, albeit statistically non-significant. Analysis across other climatic windows indicated that the 1961–1990 period exhibited a statistically significant positive trend, with snowfall increasing across the entire region. In contrast, subsequent climatic windows, 1981-1990 and 1991-2020, showed a reversal, with negative trends emerging. The negative trend was found to be statistically significant in the southwestern region during the 1981–2010 climatic window. Overall, snowfall trends remained largely negative in the last three climatic windows, covering the past 50 years since 1971, indicating a persistent decline in winter snowfall over time.

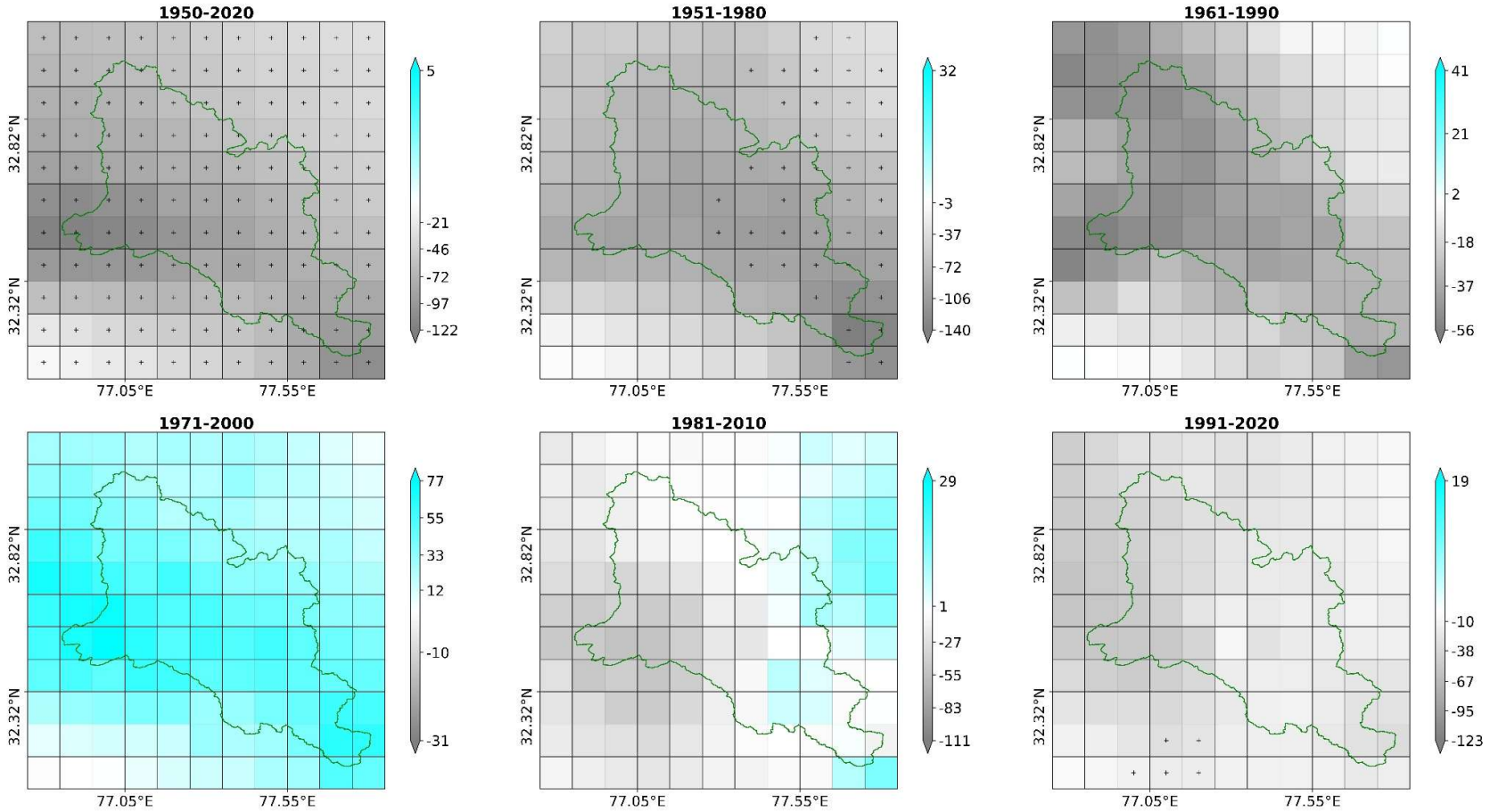

Fig. 3.11 Trend in summer snowfall, significant trends at 5% significance level are shown with dots (units in mm, w.e.)

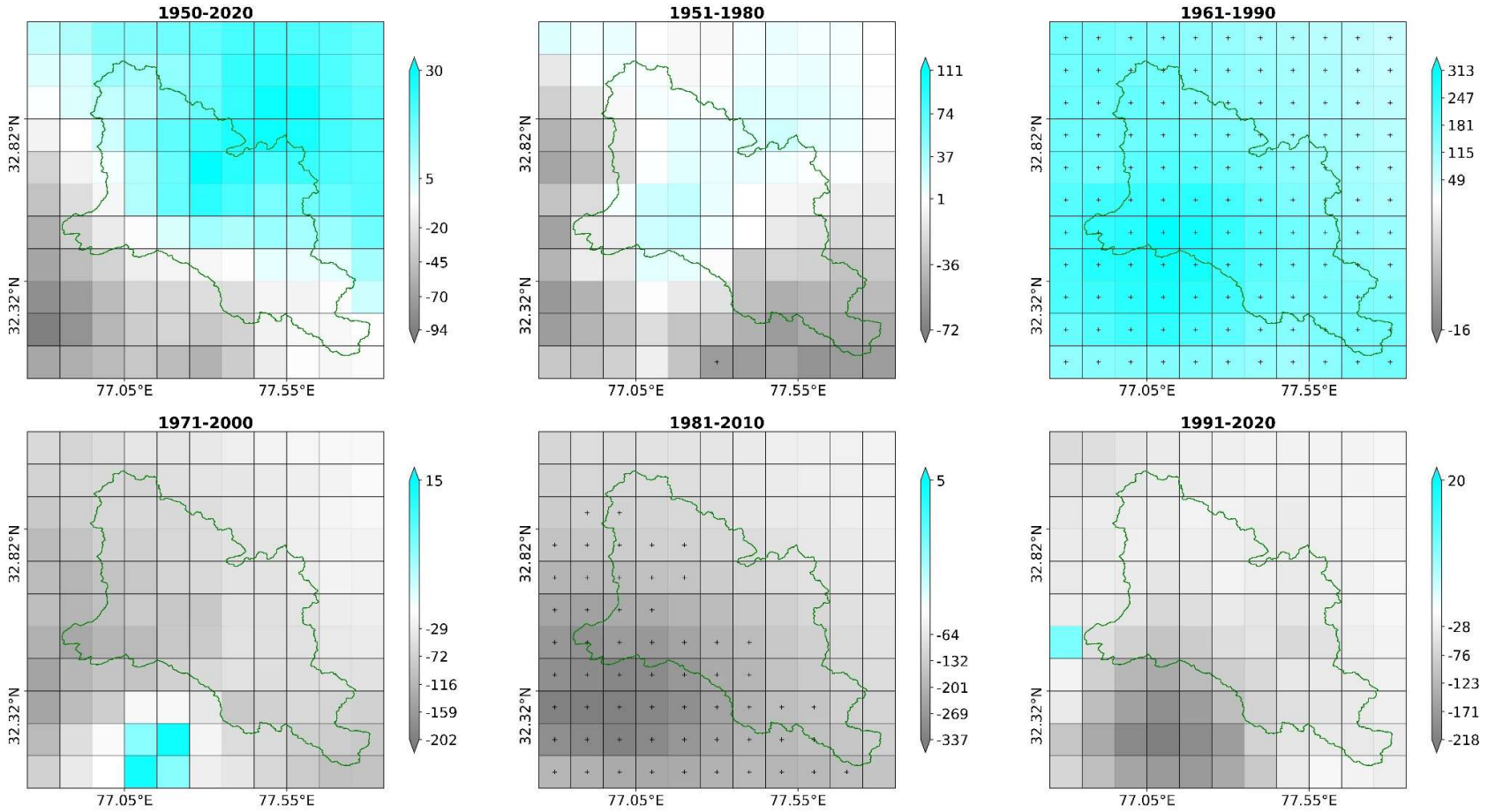

Fig. 3.12 Trend in winter snowfall, significant trends at 5% significance level are shown with dots (units in mm, w.e.)

(b) Snowfall trend in 5 year moving window

One of the most effective methods for assessing the direction of climate change is trend analysis using a moving window approach. In this study, spatial snowfall trends were also analyzed using a 5-year moving window from 1950 to 2020 (Fig. 3.13).

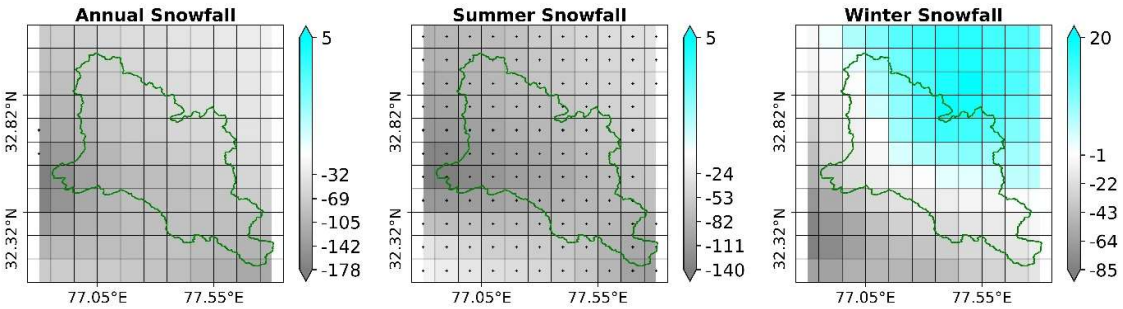

Fig. 3.13 Trend in snowfall in 5 year moving window, (units in mm, w.e.)

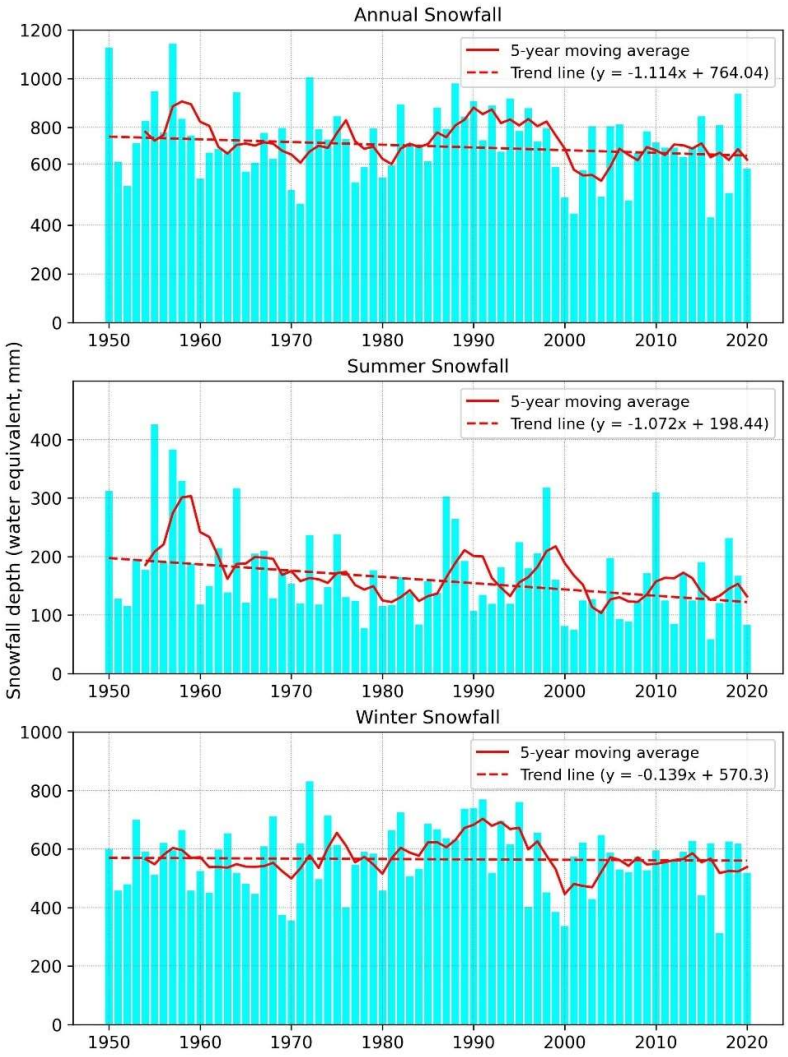

Fig. 3.14 Regional trend in annual snowfall in 5-year moving window

The annual snowfall in 5-year moving window exhibited a pronounced negative trend; however, the trends were not statistically significant. Despite this, the magnitude of change in annual snowfall over the long-term period (1950–2020) reached approximately –175 mm. Winter snowfall exhibited a mixed trend, with diametric opposing patterns along the southeast-northwest axis. While the eastern part of the region showed a positive trend, the western part experienced a negative trend for winter snowfall. However, none of these trends were statistically significant. In contrast to annual and winter snowfall, summer snowfall displayed a strong and statistically significant negative trend across the entire basin.

Besides the spatial analysis, regional snowfall trends were also evaluated by averaging the trends over the study area domain. The results indicated a negative trend for annual, winter, and summer snowfall in the 5-year moving window analysis. However, only summer snowfall demonstrated a statistically significant decline over the 1950–2020 period, highlighting a substantial reduction in snowfall during the six-month summer period. The persistent decline in summer snowfall is expected to alter downstream water availability, potentially impacting hydrological regimes and water resource management in the region.

3.4.3.2 Temperature

An analysis of ERA-5 Land temperature data was carried out for the period 1950-2020. A subset of this data, spanning the first two decades of the 21st century (2000-2020), was further examined to determine the mean monthly temperature and its variability, as illustrated in Fig. 3.15.

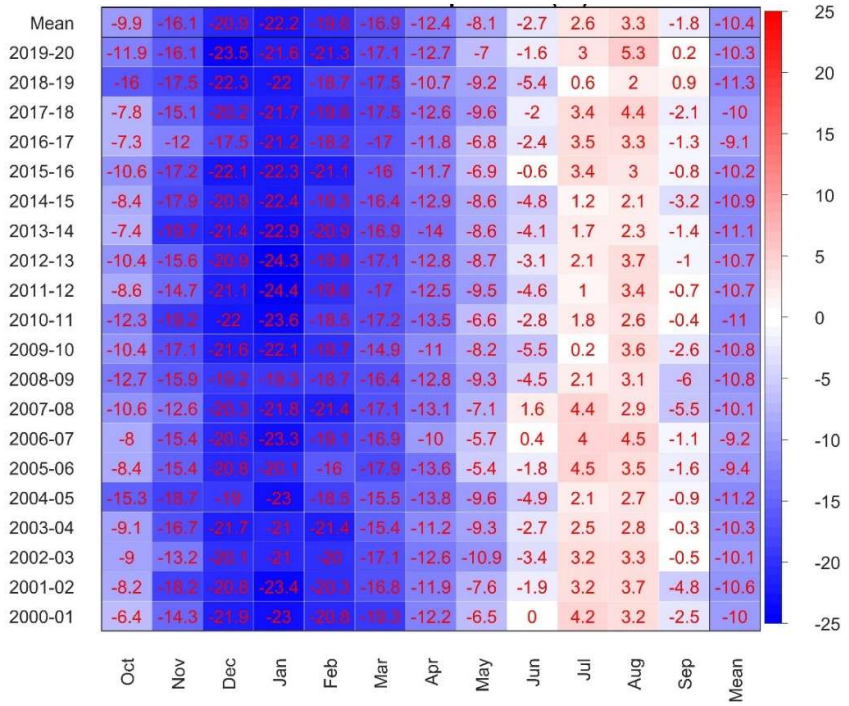

Fig. 3.15 Variation of temperature across different months during 2000-2020 in Chandrabhaga River basin as revealed by ERA5-Land data

The mean monthly temperature analysis for the Chandrabhaga River Basin from 2000 to 2020 highlights significant seasonal variations and interannual fluctuations. The annual average temperature over the study period is -10.4°C, with notable variations between years. The coldest year recorded was 2018-2019 with an annual average of -11.3°C, whereas the warmest year was 2016-2017, averaging -9.1°C. A general trend of colder conditions is evident in the early 2000s, followed by a slight warming trend in recent years.

During the winter season (November–April), temperatures remain consistently below freezing, with an average of -16.1°C in November, decreasing further to -22.2°C in January, the coldest month. December and February also exhibit low temperatures, averaging -20.9°C and -19.6°C, respectively. A gradual increase is observed from March to April, where temperatures rise from -16.9°C to -12.4°C. The winter season exhibits substantial interannual fluctuations, with certain years, such as 2009-2010 and 2010-2011, experiencing extreme cold anomalies, where temperatures in December and January dropped below -23°C. While no clear warming or cooling trend is evident for winter as a whole, variability in extreme cold events suggests shifting climatic patterns that may influence snow accumulation in the basin.

In contrast, the summer season (May–October) shows a distinct warming trend, with temperatures gradually increasing from -8.1°C in May to a peak of 3.3°C in August, before cooling again in September and October. The warmest months are July and August, with temperatures reaching up to 5.3°C (2019-2020). July and August exhibit relative stability, whereas September and October mark the transition to winter with declining temperatures. Notably, a warming trend is observed in summer months, particularly in July and August, with temperatures consistently remaining above freezing in most years. The increasing summer temperatures have significant implications for glacier melt, hydrological regimes, and water availability, as prolonged warming can accelerate ice loss and impact downstream water supply.

The analysis underscores the seasonal contrast in temperature variations, with persistent cold conditions in winter and a gradual warming trend in summer. This shifting thermal regime is likely to influence glacier dynamics, snow accumulation, and overall water balance in the Chandrabhaga River Basin, necessitating continuous monitoring and climate impact assessments.

To elucidate the temperature shift in the study area, an analysis of annual temperature anomalies was performed relative to the 1961-1990 baseline period. This enabled an assessment of the magnitude and direction of annual temperature changes with respect to the reference period. The temperature anomaly analysis relative to the 1961–1990 baseline period highlights a distinct warming trend, particularly in the post-2000 period (Fig. 3.16). Over the decades, temperature anomalies have exhibited significant interannual variability, with alternating warm and cold deviations from the baseline. However, a clear shift towards more frequent and intense positive anomalies is evident in recent years, indicating an accelerated warming trend in the Chandrabhaga River Basin.

From 1950 to 1990, temperature anomalies fluctuated, with both warm and cold phases. Several years recorded negative anomalies, suggesting cooler-than-normal conditions. Notably, 1955 (-1.35°C) and 1957 (-1.60°C) were among the coldest years, with other

significant cold anomalies occurring in 1962 (-0.96°C), 1968 (-0.92°C), and 1972 (-0.83°C). Despite these prolonged cold spells, some years, particularly from the 1970s onward, showed positive temperature anomalies, suggesting early signs of warming. The years 1980 (+1.25°C) and 1990 (+1.35°C) marked the beginning of a transition towards higher temperatures.

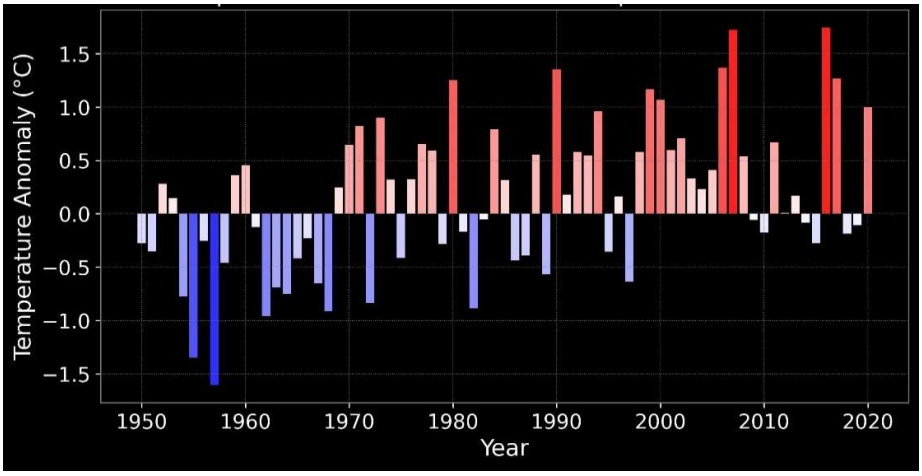

Fig. 3.16 Anomaly in regional temperature w.r.t. baseline period: 1961-1990

In contrast, the post-2000 period exhibits a sustained and intensified warming trend, with positive anomalies becoming more dominant. Unlike the earlier decades, where cold anomalies were frequent, most years after 2000 consistently recorded positive anomalies, reflecting an accelerated rise in temperatures. Some of the warmest years on record include 2016 (+1.74°C), 2007 (+1.72°C), and 2006 (+1.37°C), highlighting a significant departure from the baseline. Cold anomalies became increasingly rare during this period, with only a few instances of slight cooling, such as in 2009 (-0.06°C) and 2018 (-0.19°C).

This long-term trend signifies a transition from a mixed anomaly pattern during 1950–1990 to a predominantly warming phase from 2000 onward. The intensification of warming has critical implications for the hydrological and cryospheric systems in the Chandrabhaga River Basin. Rising temperatures are likely to alter precipitation regimes, reduce snow accumulation, and accelerate glacial retreat, directly impacting downstream water availability and hydrological cycles. These findings underscore the urgency of continued climate monitoring and adaptive strategies to mitigate the impacts of regional warming and ensure sustainable water resource management in the basin.

(a) Temperature trend

To further investigate the warming pattern in the study region, a trend analysis of the annual mean temperature was conducted over the long-term period of 1950–2020 (70 years), as well as for multiple 30-year climatic windows, namely 1951–1980, 1961–1990, 1971–2000, 1981–2010, and 1991–2020 (Fig. 3.17). The analysis revealed a statistically significant increasing temperature trend over the long-term period, indicating persistent warming in the study area.

For the first two climatic windows (1951–1980 and 1961–1990), a significant warming trend was observed, with the majority of grids within the basin exhibiting statistically

significant temperature increases. However, in the subsequent climatic windows (1971–2000, 1981–2010, and 1991–2020), the trend became more variable, with a mix of both warming and cooling patterns. Notably, during 1981–2010, a larger number of grids exhibited a statistically significant warming trend, whereas only a few grids, primarily in the southeastern part of the study area, displayed a non-significant cooling trend. Similarly, for the most recent climatic window (1991–2020), although a greater number of grids exhibited a cooling trend, none of these trends were found to be statistically significant, indicating the absence of a robust cooling pattern. Despite the climatic variability among different climatic windows, this persistent increase in temperature is expected to accelerate snowmelt and alter the hydrological regime, potentially impacting water availability and runoff patterns in the region.

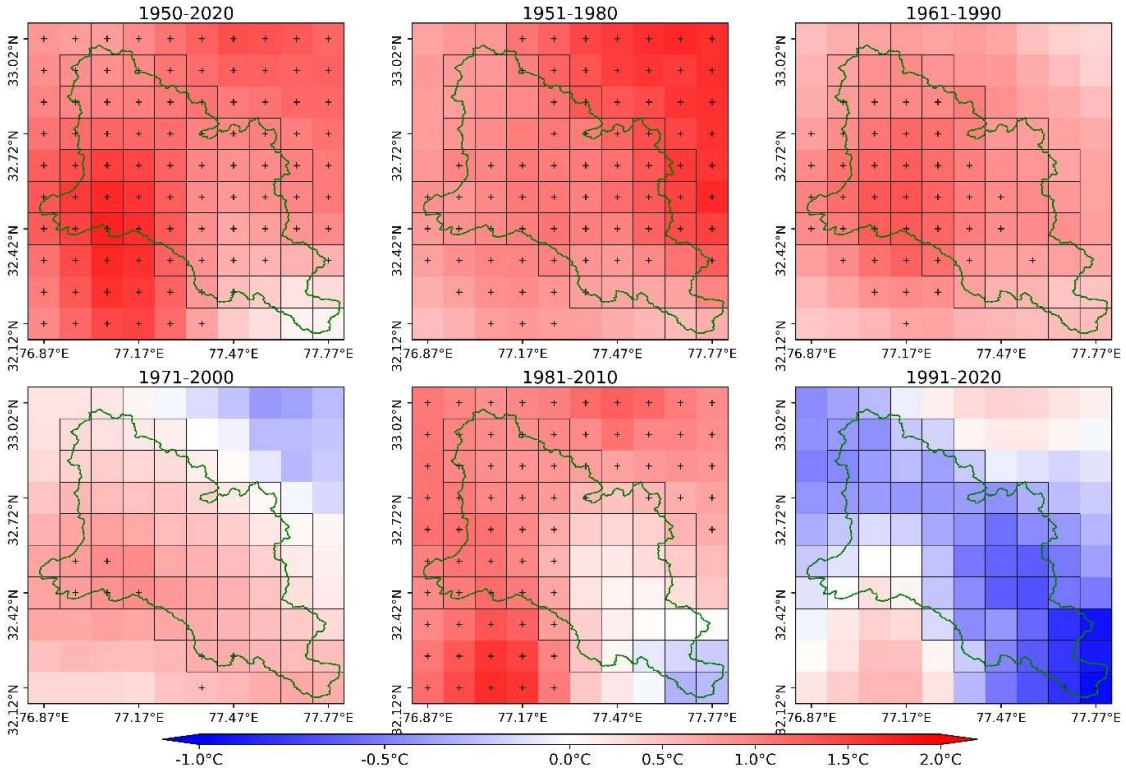

Fig. 3.17 Trend in annual average mean temperature, significant trends at 5% significance level are shown with (+) sign

(b) Temperature trend in moving window

To further assess the overall warming or cooling trends across the study domain, a 5-year moving window trend analysis was performed for the period 1950–2020 (Fig. 3.18). The analysis revealed a strong and statistically significant warming trend at the 5% significance level, suggesting a persistent rise in temperature over the study period. The convergence of significant long-term warming trends from both spatial and regional analyses confirms continuous warming in the basin.

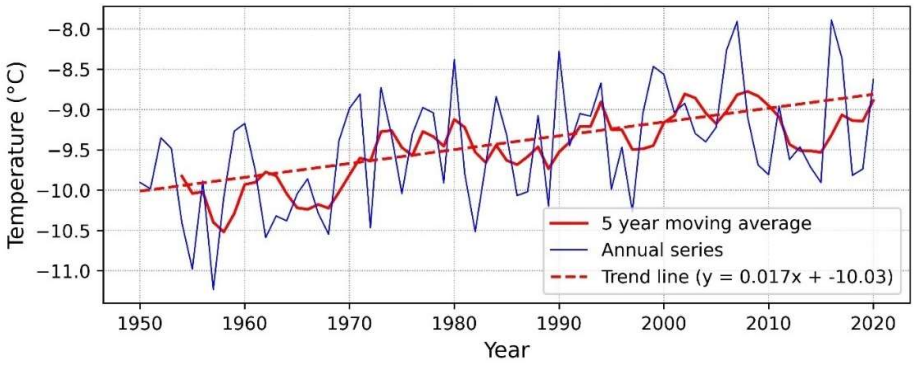

Fig. 3.18 Regional trend in annual average mean temperature in 5-year moving window

The spatial trends in annual average mean temperature, annual summer mean temperature, annual summer maximum temperature, and annual summer minimum temperature were analyzed using a 5-year moving window to assess how these trends vary spatially. As illustrated in Fig. 3.19, the analysis reveals a pronounced warming trend across the basin, with statistically significant warming observed at multiple grid points. This widespread and statistically significant increase in temperature indicates a substantial warming pattern over the region.

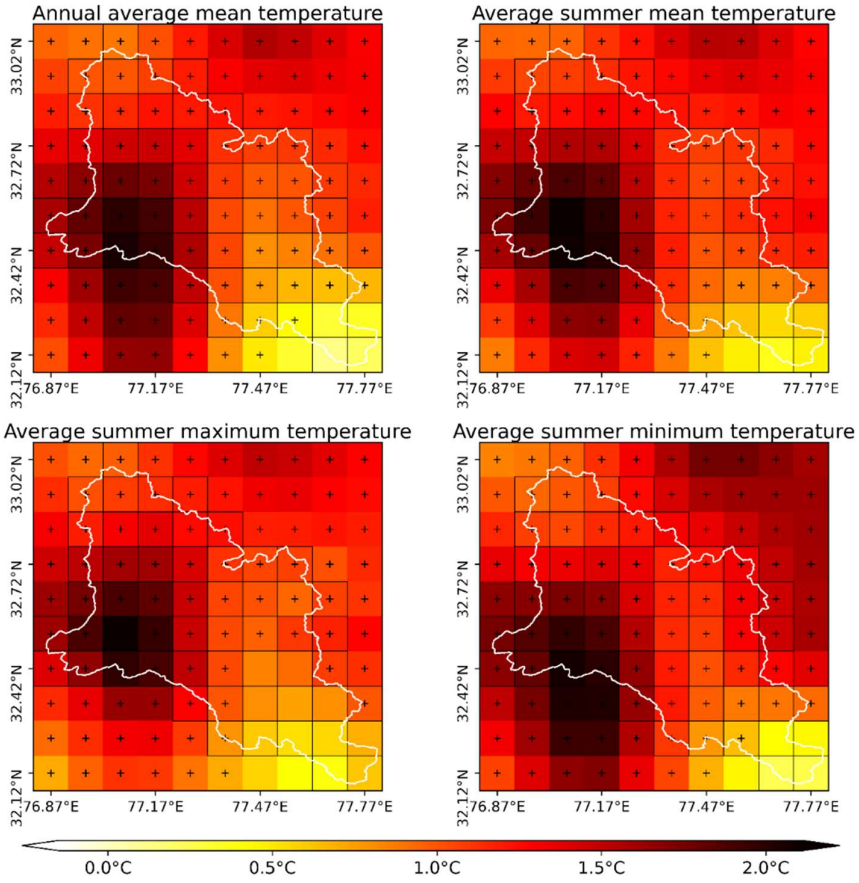

Fig. 3.19 Trend in annual average mean temperature, average summer mean temperature, average summer maximum temperature, and average summer minimum temperature in 5-year moving window, with (+) sign

Furthermore, the intensified warming during summer can be directly linked to the previously discussed significant decline in summer snowfall across the basin. The strong correlation between rising summer temperatures and decreasing snowfall suggests that temperature-driven changes in the cryosphere are playing a critical role in altering the regional hydroclimatic balance. These findings underscore the necessity for continued monitoring and modeling efforts to understand the long-term implications of warming trends on the basin's hydrological processes.

(c) Positive degree days

Positive Degree Days (PDD) refer to the cumulative sum of daily temperatures above 0°C over a given period, typically used in glaciology and hydrology to estimate snow and ice melt. The PDD approach assumes that melting is directly proportional to the amount of time and the extent to which temperatures remain above freezing. This index is widely utilized in degree-day melt models, which provide a simple yet effective way to quantify snow and glacier melt, particularly in regions where detailed energy balance data are unavailable. The significance of PDD lies in its ability to correlate temperature variations with melt rates, offering insights into seasonal and long-term changes in cryospheric processes. Increased PDD values indicate enhanced melting, often associated with climate warming and altered hydrological regimes. This has critical implications for water resource management, flood risks, and glacier mass balance studies, making PDD an essential parameter in climate change assessments and hydrological modeling.

To evaluate long-term changes in Positive Degree Days (PDD), anomalies were analyzed using a threshold of 2°C instead of 0°C. This adjustment was made to capture substantial warming conditions while reducing the influence of minor positive values in ERA5-Land reanalysis data. Similar to the previously discussed spatial trend analysis of snowfall and temperature, the trend in PDD was examined for the entire study period (1950–2020) as well as across different 30-year climatic windows, including 1951–1980, 1961–1990, 1971–2000, 1981–2010, and 1991–2020 (Fig. 3.20).

The long-term trend from 1950 to 2020 exhibited an overall increase in PDD, although only a few grid points showed statistically significant positive trends. Among the different 30-year climatic windows, a pronounced increase in PDD was observed during 1951–1980, 1961–1990, and 1971–2000, with the 1971–2000 window showing the most significant positive trend across multiple grid points. However, in the more recent climatic windows of 1981–2010 and 1991–2020, the trends were mixed. The number of grids showing a positive trend in PDD decreased in 1981–2010 compared to 1971–2000, indicating a possible shift in warming patterns. In the latest window of 1991–2020, a greater number of grid points displayed declining trends in PDD than in the preceding window, suggesting that the overall pattern of warming-driven PDD increases might be stabilizing or undergoing regional variations.

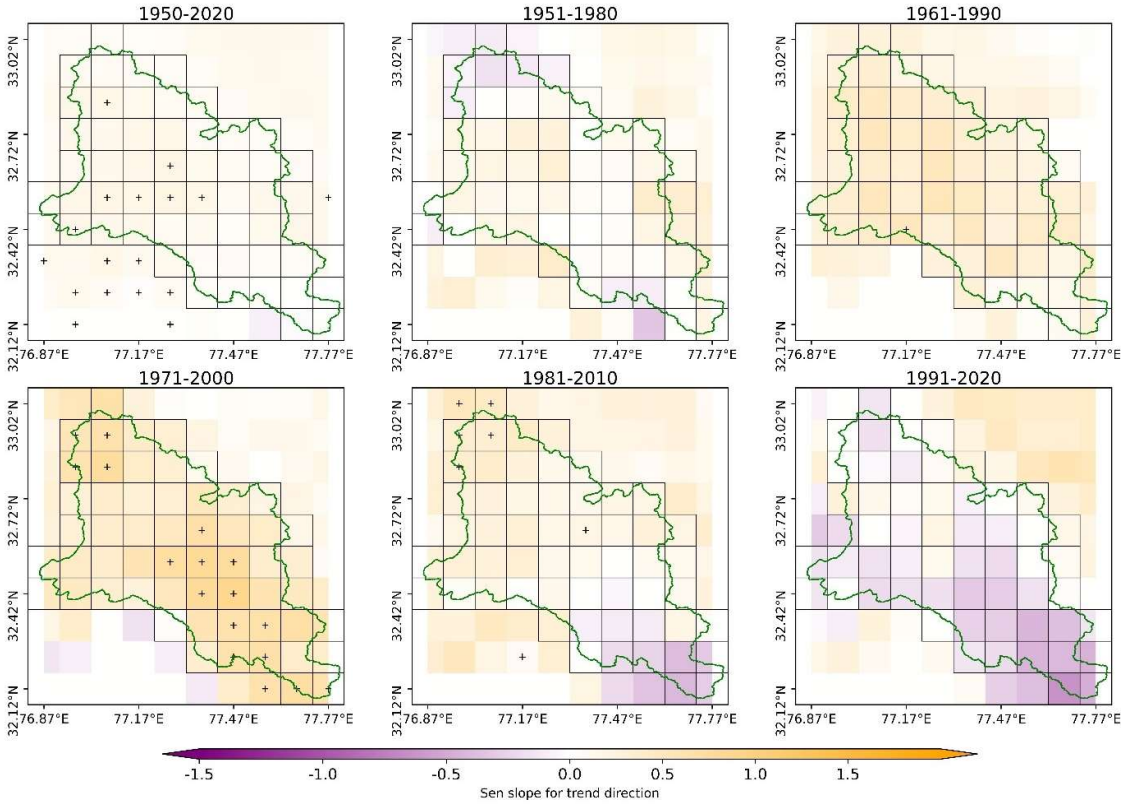

Fig. 3.20 Trend in positive degree days (>2 ºC) in summer season, significant trends at 5% significance level are shown with dots

The anomaly was calculated relative to the 1961–1990 baseline period to evaluate deviations from historical conditions. The analysis of PDD anomalies provides critical insights into warming-induced changes in snow and ice melt dynamics in the Chandrabhaga River Basin. The anomaly represents the deviation in the number of days with temperatures above 2°C, which directly influences snowmelt rates and glacier mass loss. The long-term variability in PDD anomalies exhibits substantial interannual fluctuations, with alternating periods of positive and negative anomalies before 2000 (Fig. 3.21).

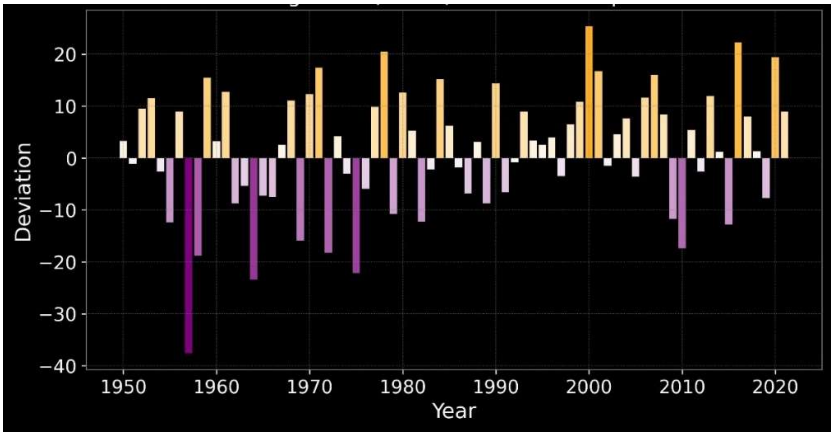

Fig. 3.21 Anomaly in positive degree days (>2 ºC) w.r.t. baseline period: 1961-1990

This suggests episodic warming and cooling phases. However, post-2000, a notable shift towards persistent and intensified warming is evident, marked by consistently positive anomalies that indicate a sustained increase in the number of warmer days conducive to snow and ice melt.

Several years post 2000 show exceptionally high positive anomalies, reflecting a significant rise in temperature-driven melting conditions. For instance, 2000 (+25 days), 2001 (+17 days), 2006 (+12 days), 2007 (+16 days), 2016 (+22 days), and 2020 (+19 days) exhibit a notable increase in PDD counts relative to the baseline. This accelerated warming trend is intensifying snowmelt processes and altering the hydrological regime of the basin. The increase in PDD anomalies post-2000 has profound implications for glacier health, streamflow seasonality, and water availability. Higher PDD counts correlate with enhanced glacier mass loss and an earlier onset of snowmelt, potentially leading to early summer runoff but reduced water availability in late summer and autumn.

These findings of PDD analysis align with the earlier discussions on temperature and snowfall trends, reinforcing the evidence of intensified warming post-2000. The increasing PDD anomalies, particularly in recent decades, highlight enhanced snowmelt conditions, which have critical implications for the hydrological balance of the Chandrabhaga River Basin.

CHAPTER 4

ESTIMATION OF SPECIFIC GLACIER MASS BALANCE

4.1 Overview

Glaciers are widely recognized as sensitive indicators of climate change, as variations in their mass balance reflect shifts in temperature and precipitation regimes over time (Aggarwal et al., 2017; Huber et al., 2020). Glacier mass balance is defined as the net gain or loss of ice from a glacier over a given period, typically reported in meters of water equivalent (m w.e.), and it serves as a key measure of glacier "health." A sustained negative mass balance (more ice loss than gain) leads to glacier thinning and retreat, signaling warming conditions, whereas a positive balance indicates growth or stability. Glaciers in the Hindu Kush–Karakoram–Himalaya (HKH) region has generally been losing mass since the late 20th century, although with significant regional variability (Berthier et al., 2024; Zemp et al., 2019). Rising air temperatures and changing precipitation patterns (including diminishing snowfall) are the primary drivers of negative mass balance in the Himalaya (Bolch et al., 2012). In the northwestern Himalaya, some studies once reported balanced or slightly positive mass balance for a few glaciers in the 1990s (Vincent et al., 2013), but more recent observations reveal accelerating ice loss in the 21st century (Hugonnet et al., 2021). The period since ~2000 in particular has seen unprecedented glacier wastage globally and in High Mountain Asia (Hugonnet et al., 2021; Zemp et al., 2019). Within the Himalaya, glaciers such as those in Himachal Pradesh (India) have experienced significant thinning and retreat (Berthier et al., 2007, 2024; Gardelle et al., 2013). However, the eastern Karakoram exhibits the so-called "Karakoram anomaly" of stable or even advancing glaciers in recent decades, highlighting spatial heterogeneity in trends (Gardelle et al., 2013) . Overall, the consensus is that Himalayan glaciers are largely in negative mass balance, contributing to reduced dry-season flows in rivers and increased proglacial lake formation(Bolch et al., 2012). In this context, consistent monitoring and modeling are crucial to quantify mass changes and understand the climatic drivers (Azam et al., 2018; Shukla et al., 2018).

Monitoring glacier mass balance is therefore critical for understanding the impacts of climate change on water resources, sea level rise, and hazard potential in mountain regions (Harrison et al., 2018; Shukla et al., 2018). However, traditional glaciological methods of measuring mass balance through stake networks and snow pit observations are labour-intensive and often unfeasible across large or inaccessible glacierized areas (Cogley, 2009). In response, researchers have increasingly turned to remote sensing and modelling approaches to estimate mass balance over broader spatial and temporal scales (Zemp et al., 2015). Two commonly used remote-sensing-based approaches for estimating glacier mass balance are the Accumulation Area Ratio (AAR) method and the Geodetic method.

The AAR method is an empirical approach that relates the fraction of a glacier's area that lies in the accumulation zone (above the equilibrium line) to its mass balance. This method provides a simplified means to infer mass-balance trends when direct measurements are sparse, and it has been applied to many glaciers worldwide (Kaser et al., 2006) and in the Himalayas

(Kulkarni et al., 2007; Pandey & Venkataraman, 2013). Decades ago, empirical studies found that many mid-latitude glaciers tend to be near equilibrium when the AAR is around 0.5–0.8, whereas AAR values significantly lower than this typically correspond to negative mass balance (Kaser et al., 2006; Zhang et al., 2018). For Himalayan glaciers, AAR-based mass balance estimation has been explored as a means to extend mass balance series or estimate balance where direct data are lacking. Kulkarni et al. (2007) successfully used satellite images to compute AAR and glacier area changes for various glaciers in the Himalaya, noting that retreating glaciers showed declining AARs over time. Pandey and Venkataraman (2013) measured changes in dozens of glaciers in the Chandra–Bhaga basin (which includes Chhota Shigri) between 1980 and 2010 using remote sensing; while their focus was on area change, such studies underscore the feasibility of using satellite data to infer glacier health metrics like AAR at basin-scale. The AAR method often involves identifying the equilibrium line altitude (ELA, the elevation at which accumulation equals ablation) on imagery (e.g., by the snowline at end of ablation season) and calculating the area above that line. Researchers have refined this technique by automating snow cover mapping using indices like the Normalized Difference Snow Index (NDSI) and applying thresholds to delineate snow vs. ice (Garg et al., 2021; Paul et al., 2004). By calibrating the relationship between AAR and mass balance using glaciers with field data, models can be developed to estimate mass balance from AAR alone (Kulkarni et al., 2007; Azam et al., 2024). Nonetheless, the accuracy of AAR-based estimates can be limited by the resolution of imagery, transient snow cover that may not equal true accumulation, and the assumption of a steady AAR–mass balance relationship over time (Kaser et al., 2006). Recent work by Azam et al. (2024) introduced a nonlinear model for Himalayan glacier mass balance (including Chhota Shigri) that can assimilate indices like AAR for improved estimates, demonstrating the evolving sophistication of the approach.

The geodetic method, on the other hand, involves comparing digital elevation models (DEMs) of a glacier's surface taken at different times to calculate volume change, which is then converted to mass change. With the increasing availability of satellite-derived DEMs, geodetic mass balance assessments have expanded across the Himalaya in recent years (Brun et al., 2017). Geodetic methods have advanced rapidly with improvements in remote sensing data. Early geodetic studies often compared a historic topographic map or the Shuttle Radar Topography Mission DEM (SRTM, from 2000) with more recent DEMs from satellite stereo-imagery (e.g., SPOT5, ASTER) or airborne LiDAR (Berthier et al., 2007; Bolch et al., 2012). For example, Berthier et al. (2007) estimated the 1999–2004 mass balance of glaciers in Himachal Pradesh (including Chhota Shigri) by differencing the SRTM DEM and a 2004 SPOT5 DEM, finding an overall negative balance and highlighting the importance of correcting for SRTM radar penetration into snow. Subsequent studies expanded geodetic assessments across the Himalaya: Gardelle et. al (2013) measured 1999–2011 changes over the entire Pamir-Karakoram-Himalaya using SRTM and SPOT5 DEMs, revealing regional patterns (significant mass loss in Himalaya, slight gains in Karakoram). In the Eastern Karakoram, Kumar et al., (2019) used SRTM (2000), ALOS (2009), and Cartosat-1 (2014) DEMs for 24 glaciers, carefully accounting for elevation-dependent bias and radar penetration, to quantify an overall slightly negative mass balance. Likewise, Muhammad et al., (2019) validated ASTER DEM differencing with field surveys in the Astore Basin (NW Himalaya),

finding near-zero mass change between 1999 and 2016, in contrast to strongly negative trends elsewhere. These studies underscore that robust co-registration of DEMs (to remove spatial biases) and corrections for factors like seasonal snow and radar penetration are critical for reliable geodetic results (Bolch et al., 2012). The availability of high-resolution data in recent years, such as sub-meter stereo satellite imagery (e.g., Pléiades) and the HMA DEMs, has improved the precision of geodetic mass balances. For Chhota Shigri specifically, Azam et al. (2016) recalculated its 2002–2014 mass balance by updating glacier hypsometry and comparing results to geodetic estimates using SPOT5 (2005) and Pléiades (2014) DEMs. They found a close agreement between the glaciological and geodetic balances (within uncertainty), reinforcing Chhota Shigri's status as a reference glacier. Srivastava et al. (2022) extended geodetic analysis to more recent years for Chhota Shigri (and a neighboring glacier), using multi-sensor DEMs to track seven decades of change. Building on these works, our study employs multiple DEM datasets (SRTM, ASTER, and Pléiades) to estimate Chhota Shigri's geodetic mass balance from 2000 up to 2024, with particular attention to minimizing uncertainties through co-registration and dataset cross-validation (Azam et al., 2024; Mandal et al., 2024)

Each method has its strengths and limitations: the AAR approach is straightforward and can use optical satellite imagery to frequently update mass balance proxies, but it relies on empirical relationships and requires calibration; the geodetic approach provides a more direct measurement of ice volume change distributed over the glacier, but it typically represents multi-year averages and requires careful error correction (Gardelle et al., 2013; Kumar et al., 2019). By synthesizing the AAR and geodetic approaches, the study aims to provide a comprehensive picture of Chhota Shigri Glacier's mass balance. Previous studies integrating in situ, AAR, and geodetic data suggest that such multi-method analyses can greatly improve confidence in the results and help attribute differences to methodological or climatic causes.

Present work builds on this foundation by explicitly comparing the AAR-derived mass balance indicators (such as changes in accumulation area and ELA) with the volumetric changes observed from DEM differencing. This comparative framework is expected to yield insights into not only how much mass Chhota Shigri has lost, but also the processes and patterns of change (e.g., whether mass loss is driven more by reduction in accumulation or increased ablation in certain periods).

4.2 Methodology

This study employs two distinct methodologies to estimate the mass balance of Chhota Shigri Glacier from 2000 to 2024: (1) a remote sensing approach based on Accumulation Area Ratio (AAR) and related Equilibrium Line Altitude (ELA) analyses, and (2) a Geodetic approach based on DEM differencing. Satellite imagery and DEM datasets were processed using a combination of Google Earth Engine (for image processing), GIS software, and statistical analysis tools. The AAR method involves delineating glacier accumulation vs. ablation areas on multi-temporal optical images and computing the ratio, which is then related to mass balance through empirical calibration. The geodetic method involves obtaining multiple DEMs, aligning them in a common reference frame, subtracting elevations to get

thickness changes, and converting to mass change. Below, we detail each methodology separately.

4.2.1 AAR-Based Methodology

4.2.1.1 Data and Preprocessing

This study utilizes Google Earth Engine to examine glacier mass balance using remote sensing. Landsat images are filtered spatially and temporally, and a 30m SRTM DEM is loaded and masked with a snow mask. Glacier boundaries are digitized for multiple years, and a snow mask is generated. The Normalized Difference Snow Index (NDSI) is computed and threshold to classify snow cover, estimating the AAR. Snow cover area and cumulative area are calculated, followed by mass balance modelling using correlation analysis between AAR and non-linear calibrated mass balance (NLMB) taking calibration period (2003-2019), validation period (2020-2023) and estimation period (2000-2002 & 2024). Correlation analysis and mass balance equations are applied before exporting final results. The overall methodology is shown in Fig. 4.1.

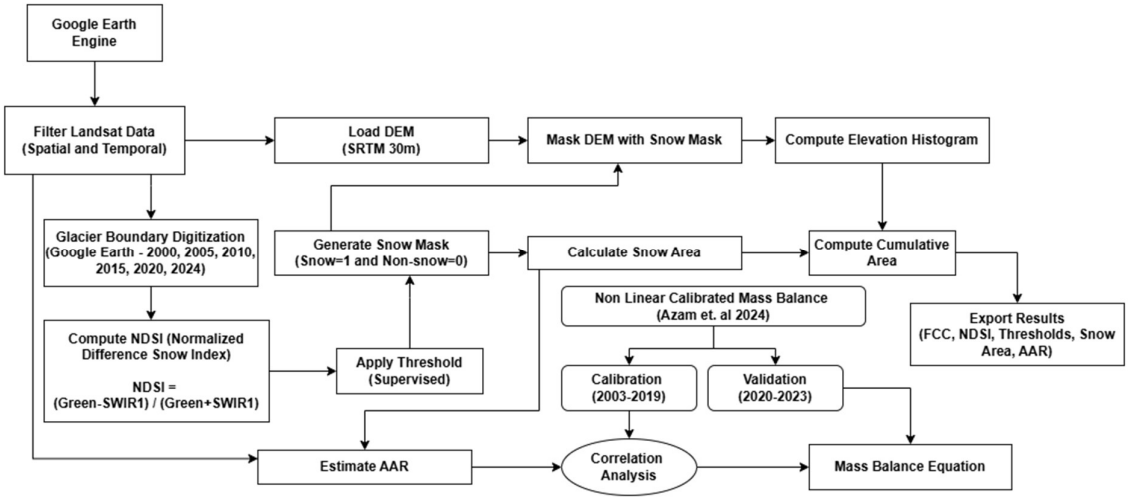

Fig. 4.1 Methodology Chart

4.2.1.2 Glacier Boundary Digitization (2000-2024)

The glacier outline was updated for each selected year (2000, 2005, 2010, 2015, 2020, and 2024) using multi-temporal Landsat images to assess changes in glacier extent over time. These satellite images were carefully chosen from the August to October period to minimize the influence of cloud cover and transient snow, thereby enabling accurate mapping of the glacier boundary. Table 4.1 provides a summary of the satellite datasets utilized. An integrated approach combining on-screen visual interpretation and automated digital classification techniques was adopted. This included the application of band ratios (e.g., TM4/TM5), spectral indices such as the Normalized Difference Snow Index (NDSI) and the Normalized Difference Glacier Index (NDGI), as well as band composites and contrasting techniques (Bolch & Kamp, 2006; Paul et al., 2004).

Table 4.1 The Information of Landsat satellite imageries

Landsat Imagery	Year/Date	Path/Row
SRTM DEM	**2000**	
Landsat 5	28-08-2000	147/38
Landsat 5	24-09-2001	147/38
Landsat 5	10-05-2002	147/38
Landsat 7	22-09-2003	147/38
Landsat 7	08-09-2004	147/38
Landsat 7	26-08-2005	147/38
Landsat 7	30-09-2006	147/38
Landsat 7	16-08-2007	147/38
Landsat 7	03-09-2008	147/38
Landsat 7	21-08-2009	147/38
Landsat 7	09-09-2010	147/38
Landsat 7	20-09-2011	147/38
Landsat 8	17-09-2013	147/38
Landsat 8	27-08-2014	147/38
Landsat 8	30-08-2015	147/38
Landsat 8	16-08-2016	147/38
Landsat 8	04-09-2017	147/38
Landsat 8	22-08-2018	147/38
Landsat 8	10-09-2019	147/38
Landsat 8	12-09-2020	147/38
Landsat 8	30-08-2021	147/38
Landsat 8	02-09-2022	147/38
Landsat 8	20-08-2023	147/38
Landsat 8	22-08-2024	147/38

The initial delineation of the glacier was performed using a clean ice mask generated through the TM4/TM5 band ratio, which was then refined manually to correct for misclassified regions such as shadows, rock outcrops, or debris-covered ice. Further refinement was achieved using false-colour composites of the NIR, Red, and Green bands, leveraging the spectral reflectance differences between glacier ice and surrounding terrain to improve boundary accuracy. The classification scheme recommended by the Global Land Ice Measurements from Space (GLIMS) (http://www.glims.org/MapsAndDocs/guides.html) initiative was followed to ensure consistency in glacier mapping practices (Bolch & Kamp, 2006; Kulkarni et al., 2007). This included incorporating debris-covered ice within the glacier outline and excluding proglacial lakes and surrounding non-glacial features.

To enhance boundary precision, the delineated glacier outlines were cross-validated using the Shuttle Radar Topography Mission (SRTM) Digital Elevation Model (DEM), which enabled visualization of glacier flow paths and topographic lows typically occupied by glacier ice. The final corrected glacier boundaries were imported into ArcGIS for area calculations. The glacier snout (terminus) position for each year was determined by identifying the lowest

elevation point of the glacier outline and was further validated using a combination of methods, including the interpretation of proglacial stream origin and the location of terminal moraines, as suggested by Murtaza and Romshoo (2016). The glacier changes in length and area between 2000 and 2024 were quantified using delineated outlines. Snout retreat distances were measured along a central flowline by comparing the positions of the glacier terminus across successive years. Total area change was determined by calculating the difference in glacier extent between 2000 and 2024, with intermediate changes also documented. These geometric indicators serve as independent evidence of glacier evolution and offer a means of validating the mass balance results, as sustained negative mass balances are generally associated with reductions in glacier area and length.

4.2.1.3 Snow Cover and AAR Calculation

The core of the AAR method is separating the accumulation area from the ablation area on the glacier for each year. For this the Normalized Difference Snow Index (NDSI) was utilized to map snow-covered vs. bare-ice areas on the glacier surface (Eq. 1).

$$NDSI = \frac{(Green - SWIR)}{(Green + SWIR)} \qquad \textbf{Eq. 1}$$

For each satellite image, the Normalized Difference Snow Index (NDSI) was calculated and a threshold was applied to differentiate snow-covered surfaces (characterized by high NDSI values) from ice or debris (with lower NDSI values). Visual inspection of histograms indicated that a threshold value in the range of approximately 0.4 to 0.5 was generally effective in separating bright snow from darker ice and debris. However, to enhance accuracy, manual adjustments were performed to select a threshold that best aligned with the visually interpreted snowline in each image. Due to differences in lighting conditions and sensor characteristics among Landsat missions, the optimal NDSI threshold varied slightly from image to image, typically ranging between 0.4 and 0.8. Following thresholding, a binary snow cover mask was generated for each image. This mask was overlaid on the delineated glacier outline to extract the area classified as snow-covered (representing the accumulation area) and the area without snow cover (interpreted as the ablation zone). Isolated patches of snow observed at lower elevations—likely representing residual avalanche deposits—were individually assessed and, if necessary, excluded from the accumulation area to avoid classification errors. In cases where snow patches were missed by the automated thresholding due to low reflectance or shadow effects, manual inclusion was performed to ensure completeness. After finalizing the accumulation area, the Accumulation Area Ratio (AAR) was computed using the formula (eq. 2):

$$AAR = \frac{Accumulated\ Area}{Total\ Glacial\ Area} \qquad \textbf{Eq. 2}$$

This yielded an AAR value for each of the six years considered. In addition, the approximate ELA corresponding to the delineated accumulation area was identified. This was achieved by extracting the mean elevation along the boundary separating snow-covered and snow-free ice on the glacier surface. The boundary was represented as a polyline derived from

the edge of the snow cover mask, and elevation values were sampled along this line using the digital elevation model (DEM). The average or median of these elevation values was recorded as the ELA for the respective year, following the approach outlined by Kulkarni et al. (2007). Where available, these remotely sensed ELAs were compared with in situ ELA observations (e.g., from stake networks) to facilitate validation and improve confidence in the result.

4.2.1.4 Mass Balance Estimation from AAR

The Accumulation Area Ratio (AAR) serves as an indicator of relative glacier health, with higher AAR values generally associated with more favourable (i.e., less negative or positive) mass balance conditions. In this study, a calibration procedure was implemented to convert AAR values into quantitative mass balance estimates. This process involved developing a relationship between satellite-derived AAR and annual glacier mass balance using the long-term glaciological record of Chhota Shigri Glacier (Azam et al., 2018) along with modelled mass balance data (Azam et al., 2024). For the years 2002 to 2019 (excluding data gaps), AAR values—estimated from late ablation season satellite imagery—were paired with corresponding glaciological mass balance measurements to establish this relationship.

Given the evidence of non-linearity between AAR and mass balance, as emphasized by Azam et al. (2024), a polynomial regression approach was adopted. Specifically, estimated AAR values were correlated with the calibrated nonlinear model-based mass balance data for the period 2003–2019, which served as the testing phase. A polynomial equation was generated from this correlation, effectively capturing the non-linear relationship between AAR and mass balance for the glacier. This derived equation was subsequently applied to estimate and validate mass balance for the years 2020–2023, providing a consistent framework for extending the mass balance series using remote sensing-derived AAR values.

In brief, the AAR methodology integrated remote sensing of snow cover—using NDSI thresholding applied to Landsat imagery—with elevation data from a digital elevation model (DEM) to estimate the equilibrium line altitude (ELA) and the accumulation area. This enabled the calculation of AAR values for multiple time periods. By calibrating these values against established mass balance datasets, approximate mass balance trends for Chhota Shigri Glacier were derived. The approach leverages the relatively high temporal availability of optical satellite imagery to capture interannual variations in glacier behavior, while acknowledging the empirical nature of the estimation. The outcomes from this method are interpreted in conjunction with observed geometric glacier changes and compared against results obtained from the independent geodetic method described in the subsequent section.

4.2.2 Geodetic Methodology

The geodetic method for estimating glacier mass balance involves a structured sequence of steps to ensure accuracy and consistency (Fig. 4.2). Initially, all DEM datasets are reprojected and resampled to a common spatial reference and resolution. Seasonal snow cover is corrected using optical imagery, followed by applying radar penetration correction,

particularly for SRTM data. Co-registration is then performed to align DEMs using stable terrain. Elevation change is calculated by differencing DEM pairs for defined intervals, with outlier values removed to avoid artifacts. Finally, volume changes are converted to mass changes using standard ice density values, allowing the computation of specific mass balance over time.

Fig. 4.2 Methodology for Geodetic Mass Balance Calculation

To estimate the geodetic mass balance of Chhota Shigri Glacier, a suite of Digital Elevation Models (DEMs) with approximately 30 m horizontal resolution was compiled for the period 2000 to 2024. The primary DEMs utilized include:

4.2.2.1 SRTM C-band DEM (February 2000):

This DEM served as the baseline elevation surface. The Shuttle Radar Topography Mission (SRTM) provides near-global coverage at a native resolution of 1 arc-second (~30 m). To address voids and elevation inaccuracies in steep terrain and snow/ice regions, the processed and void-filled version 3 product was used.

4.2.2.2 ASTER 14DMO DEMs (2009 and 2015):

Derived from ASTER stereo image archives by METI/NASA, these DEMs represent multi-year averages centered around 2009 and 2015. Selected from the ASTER Global DEM (GDEM) mosaic at 1 arc-second (~30 m) resolution, these datasets served as intermediate time points.

4.2.2.3 Pléiades DEM (2020):

Pleiades DEM (2020) was sourced from the Pleiades Glacier Observatory (PGO), an initiative by CNES (French Space Agency) and LEGOS. The PGO dataset includes high-resolution (2 m and 20 m) DEMs, along with 0.5 m panchromatic and 2 m multispectral ortho-images, facilitating detailed glacier surface analysis (Berthier et al., 2024). A high-resolution (2 m) DEM generated from Pléiades stereo imagery acquired in September 2020 was employed (Azam et al., 2024). For consistency, this dataset was downsampled to 30 m, though its high vertical accuracy was retained to support reliable reference surface generation for recent glacier conditions.

4.2.2.4 ASTER L1A DEM (2024):

ASTER DEMs was generated using the MicMac ASTER (MMASTER) tool (Girod et al., 2017), which processes stereoscopic imagery captured by ASTER's nadir-looking (Band 3N) and backward-looking (Band 3B) telescopes. The tool refines Rational Polynomial Coefficients (RPCs) derived from ASTER metadata, enhancing image matching quality and

mitigating cross-track parallax errors caused by satellite jitter (Girod et al., 2017). Compared to the standard NASA DEM product (AST14DMO), which is generated using the SilcAst software, MMASTER-generated DEMs exhibit reduced noise and fewer unmatched areas, thus improving accuracy and data coverage. This methodology has been widely applied in contemporary glaciological studies (Das et al., 2022; Hugonnet et al., 2021).

All DEMs were reprojected to a common spatial reference frame (UTM Zone 43N, WGS84 datum) and resampled to a uniform grid. A 1–2 km buffer zone around the glacier was retained for co-registration and bias assessment, although the main analysis was restricted to the glacierized area.

4.2.2.4 Co-registration and Elevation Difference:

For removing the vertical and horizontal offset, both the DEMs were co-registered using the method described by (Berthier et al., 2007), which was inspired by (Rodríguez et al., 2006). A horizontal shift between the DEMs can significantly increase the standard deviation of their elevation differences without necessarily affecting the mean. The approach involves iteratively shifting a slave DEM in small increments until the standard deviation of the elevation difference reaches a minimum. This procedure is implemented using IDL, the programming language bundled with ENVI. The IDL algorithm utilizes stable, non-glaciated areas to co-register DEMs, ensuring accurate alignment. These stable areas are identified using RGI glacier boundaries. A mask file is created on the basis of these stable regions, ensuring that only non-glacial terrain is used for co-registration. This mask is then applied during the DEM alignment process, minimizing errors caused by glacier surface changes and improving the accuracy of elevation difference calculations.

Before elevation difference estimation, the DEMs were also corrected for radar penetration bias. Most of the DEMs were acquired close to the end of the hydrological year, reducing the impact of any seasonal offset. For DEMs acquired at other times of the year, seasonality corrections were applied to account for temporal variations. For the other western study sites (Pamir, Hindu Kush, and Spiti Lahaul), the seasonality correction is based on the mean winter mass balances of 35 glaciers in the Northern Hemisphere, which averaged +0.89 m w.e. per year from 2000 to 2005. This corresponds to a seasonal rate of +0.15 m w.e. per winter month (Ohmura, 2011).

The co-registered DEMs were then differenced (ΔDEM) to generate an elevation change map at the pixel level over the glaciated terrain. This elevation change is then converted to volume change by multiplying it with the glacier area as shown in Eq. 3.

$$\boldsymbol{Volume\ change = \Delta DEM \times glacier\ area} \qquad \textbf{Eq. 3}$$

The volume change is then converted into glacier mass change (Eq. 4) using a density conversion factor of 850 kg m^{-3}.

$$\boldsymbol{Mass\ Balance = \frac{Volume\ change \times 850}{1000 \times Glacier\ area}} \qquad \textbf{Eq. 4}$$

Elevation changes greater than +100 m or less than -100 m were typically treated as outliers, as these values often correspond to data gaps or DEM edges. Additionally, pixels with

absolute elevation differences exceeding three standard deviations from the mean within each altitude bin were also discarded, ensuring that only the most reliable data are considered for further analysis.

4.2.2.5 Uncertainty assessment

The uncertainties in geodetic mass balance estimates arise from various factors, including errors in DEM differencing, radar signal penetration, void filling in source DEMs, glacier outline delineation, and the use of a single value for ice density in mass conversion. These factors were accounted for in the uncertainty assessment, following the methodology of (Huber et al., 2020). A constant value of ± 60 kg m^{-3} was used to account for the uncertainty associated with the volume to mass conversion. The standard deviation of elevation differences over the stable terrain was used as the uncertainty in elevation change, assuming no actual elevation change should occur in these areas. For the uncertainty in glacier area, a relative uncertainty of 3% of the total mapped glacier area was assumed, following common practice in glacier studies. The cumulative errors due to all the three factors were taken into account for the glacier mass change estimates.

In addition to the uncertainty in glacier elevation change ($\delta\Delta h$), the uncertainties in glacier area (δA) and density assumption (δρ) are also considered when estimating the overall mass change uncertainty (δΔM). It is calculated using the following equation (Eq. 5):

$$\boldsymbol{\delta_{\Delta M}} = |\boldsymbol{M}| \times \sqrt{\left(\frac{\delta_{\Delta h}}{\Delta h}\right)^2 + \left(\frac{\Delta a}{A}\right)^2 + \left(\frac{\delta \rho}{\rho}\right)^2} \qquad \textbf{Eq. 5}$$

Where, ΔM = Total mass change (kg or Gt)

Δh = Mean Elevation Change (m)

A = Glacier Area (m^2)

ρ = Density of volume change (kg/m)

$\delta_{\Delta h}$ = Uncertainty in elevation change (m)

δ_A = Uncertainty in glacier area (m^2)

δ_ρ = Uncertainty in density (kg/m^3)

This formula accounts for uncertainty associated with mean elevation difference, glacier area and conversion density; ensuring a comprehensive assessment of uncertainties in the geodetic mass balance calculations.

4.3 RESULTS AND DISCUSSION

In this section, the findings from the AAR-based analysis and the geodetic DEM analysis are presented, and their implications are discussed. For clarity, results from each method are discussed separately, followed by an integrative comparison. Both methods consistently indicate that Chhota Shigri Glacier has undergone significant mass loss from 2000

to 2024, although the magnitude and temporal pattern of this loss provide interesting insights when examined method-wise.

4.3.1 AAR Method Results

4.3.1.1 Glacier Boundary Digitization (2000-2024) result:

The glacier boundary was delineated using Landsat satellite imagery, employing various band combinations to enhance the visual distinction of snow and ice-covered areas. All satellite images were acquired between August and October, a period selected to minimize the influence of peak snowfall and to best represent the end-of-ablation season conditions for accurate glacier mapping (Fig. 4.3).

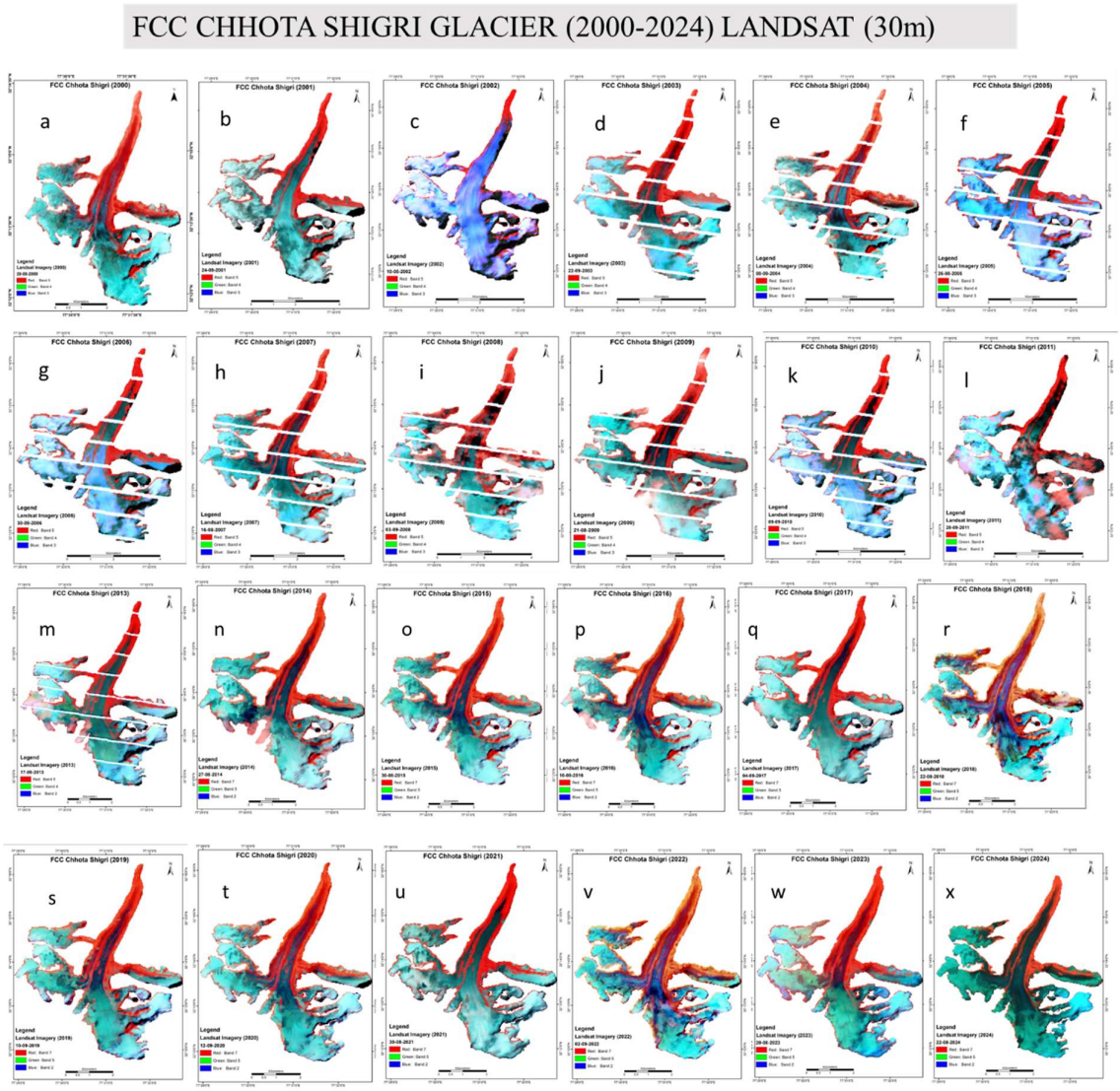

Fig. 2.3 FCC map of Chhota Shigri glacier a. 2000, b. 2001, c. 2002, d. 2003, e. 2004, f. 2005, g. 2006, h. 2007, i. 2008, j. 2009, k. 2010, l. 2011, m. 2013, n. 2014, o. 2015, p. 2016, q. 2017, r. 2018, s. 2019, t. 2020, u. 2021, v. 2022, w. 2023, x. 2024

Delineation of Chhota Shigri's outline on the Landsat images revealed a steady reduction in glacier area over the 24-year study period (Fig 4.4). In 2000, the glacier's area was measured at approximately 15.93 km². By 2024, the area had decreased to about 15.36 km². This corresponds to a total area loss of ~0.57 km², or roughly 3.6% of the 2000 area. The shrinkage was not linear in time; the glacier lost about 0.05–0.1 km² per interval of five years, with slightly larger losses in the first decade. The glacier terminus has retreated markedly.

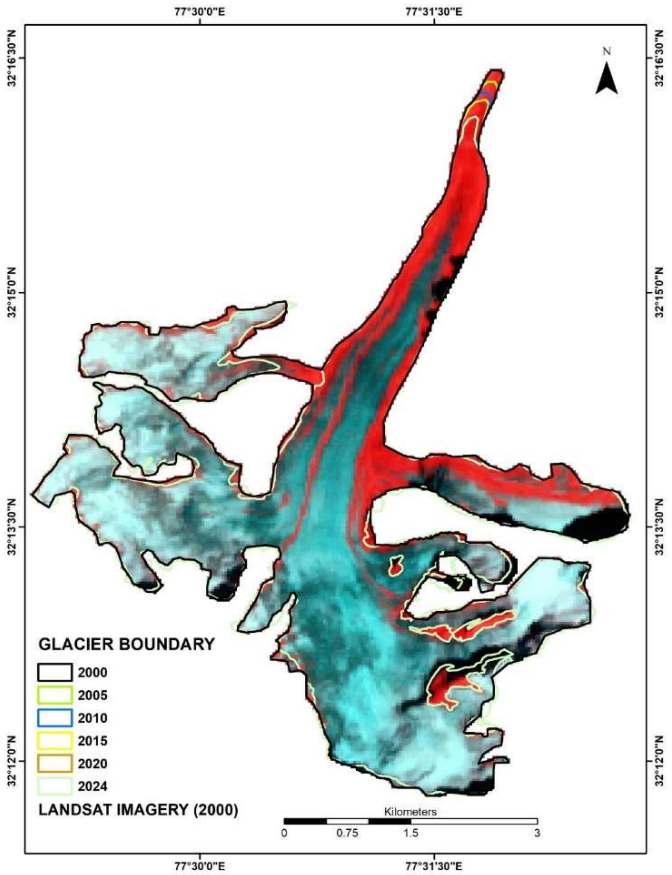

Fig. 4.4 Snout Retreat of Chhota Shigri Glacier

Table 4.2 summarizes the measured snout retreat distances in three sub-periods. The largest retreat occurred between 2000 and 2015, when the terminus pulled back about 252 m up-valley, rising from ~4050 m to ~4072 m elevation. From 2015 to 2020, an additional ~235 m of retreat was observed, with the snout altitude reaching ~4130 m. The early 2020s saw a somewhat reduced retreat rate – from 2020 to 2024 the terminus receded ~90 m further, ending around ~4135 m elevation. In total, the glacier's length shortened by roughly 577 m over 24 years. The upward shift of the terminus by ~85 meters of elevation (4050 m → 4135 m) indicate significant down wasting. Field observations in past studies support these magnitudes; for instance, Azam et al. (2012) noted notable retreat and surface thinning in the 2000s. The presence of thick debris at the toe may slow down terminus retreat somewhat (insulating effect), which could explain the slightly lower retreat rate in the last interval despite continued mass loss.

Table 4.2 Snout (terminus) retreat of Chhota Shigri Glacier in different periods, based on remote sensing delineation.

Period	Retreat Distance (m)	Snout Elevation (m a.s.l.) (start → end)
2000–2015	252 m	4050 - 4072 m
2015–2020	235 m	4072 - 4130 m
2020–2024	90 m	4130 - 4135 m

4.3.1.2 Snowline (ELA) and AAR Observations:

Using the Normalized Difference Snow Index (NDSI) approach on selected late-summer satellite images, the annual snow-covered area on Chhota Shigri Glacier was delineated and interpreted as the seasonal accumulation area. Based on the automated snowline analysis using NDSI, the Equilibrium Line Altitude (ELA) for Chhota Shigri Glacier was estimated (Table 4.3) for each year from 2001 to 2024, with the exception of 2012, for which no data were available. The ELA values show significant interannual variability, ranging from a low of 4995 m in 2001 to peaks of 5076 m in both 2002 and 2023. During the early 2000s (2001–2006), the ELA generally remained below 5050 m, indicating relatively favourable mass balance conditions. In 2010, a relatively low ELA of 5004 m was observed, suggesting a positive mass balance year with substantial snow retention. From 2011 onwards, the ELA fluctuated within a narrow band of 5000–5060 m, with 2013 (5003 m), 2015–2016 (5035 m), and 2018 (5019 m) representing relatively moderate conditions. Higher ELAs in 2019 (5059 m), 2020 (5052 m), and especially 2023 (5076 m) suggest recent years have seen reduced accumulation areas and more negative mass balance trends. The data also show a slight rising trend in ELA over the 24-year period, particularly during the 2020s, indicating increasingly negative glacier mass balance conditions. The recurrence of ELAs above 5050 m in the most recent years aligns with broader climatic observations of warming and reduced glacier health in the region. These remote-sensing-derived ELAs are broadly consistent with previously reported field-based values for Chhota Shigri and reinforce the interpretation of a persistent mass loss trend over the study period.

Table 4.3 ELA Comparison of Chhota Shigri Glacier

Year/Date	Snowline/ELA Automated	ELA Calibrated
24-09-2001	4995	No-Data
10-05-2002	5076	No-Data
22-09-2003	5052	5145
08-09-2004	5027	5156
26-08-2005	5019	4911
30-09-2006	5012	5157
16-08-2007	5027	5128
03-09-2008	5059	5096
21-08-2009	5043	4942
09-09-2010	5004	4921
20-09-2011	5027	5022
2012	NA	5061
17-09-2013	5003	5131
27-08-2014	5035	5004

Year/Date	Snowline/ELA Automated	ELA Calibrated
30-08-2015	5035	5027
16-08-2016	5035	5148
04-09-2017	5043	5151
22-08-2018	5019	5167
10-09-2019	5059	4930
12-09-2020	5052	5125
30-08-2021	5035	5013
02-09-2022	5027	5248
20-08-2023	5076	4985
22-08-2024	5059	NA

The supervised NDSI threshold and corresponding AAR values from 2000 to 2024 reveal significant interannual variability, reflecting changing glacier accumulation conditions over time (Fig. 4.5). The NDSI thresholds applied ranged from 0.41 to 0.91, with lower thresholds typically observed in years with extensive snow cover, such as 2005 and 2009 (both with thresholds of 0.41), corresponding to high AAR values of 0.72 and 0.63, respectively. Conversely, years with high thresholds (e.g., 2020 and 2017, with thresholds above 0.9) were associated with lower AAR values, indicating limited accumulation area and dominant ablation conditions. Notably, 2022 had an AAR of only 0.23 despite a high threshold of 0.87, highlighting one of the poorest accumulation seasons in the record. The overall pattern suggests a general decline in AAR values in the latter years, with occasional recoveries, such as in 2019 (AAR = 0.65) and 2021 (AAR = 0.59). These observations underscore the sensitivity of snow cover dynamics to annual climatic conditions and validate the supervised NDSI approach as a reliable method for mapping seasonal glacier accumulation extent.

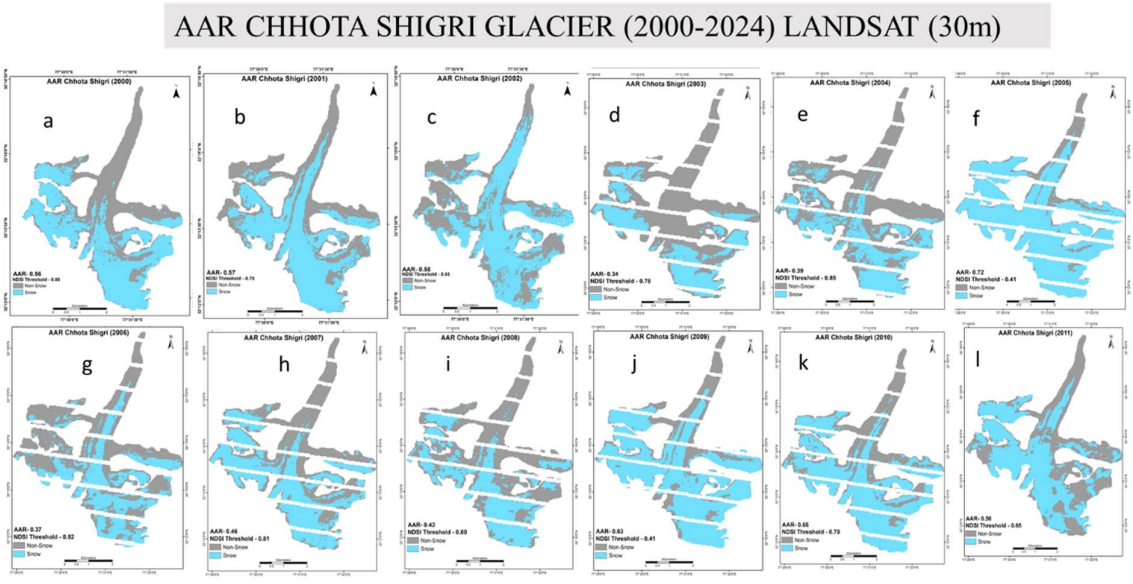

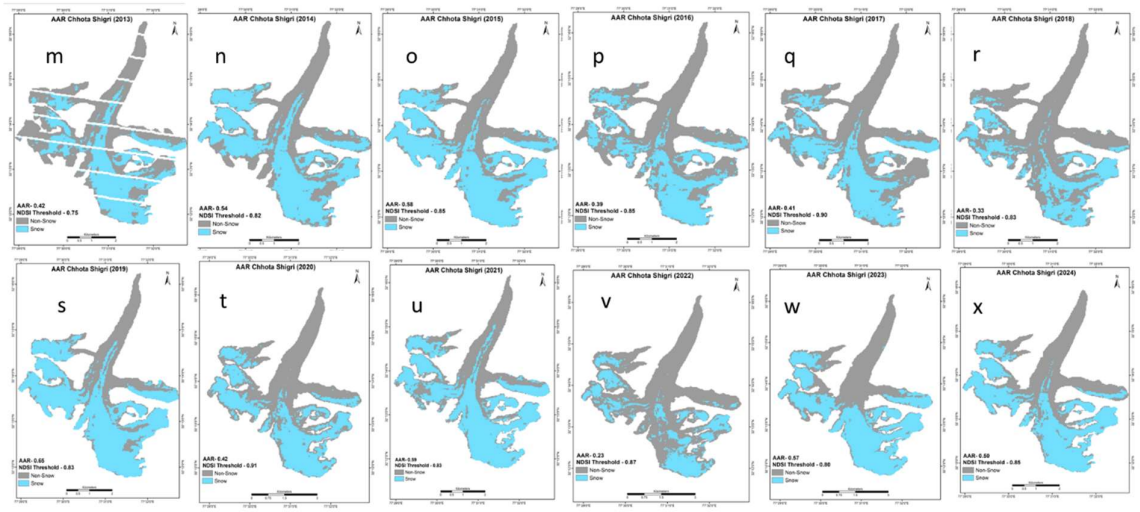

Fig. 4.5 AAR map of Chhota Shigri glacier: a. 2000, b. 2001, c. 2002, d. 2003, e. 2004, f. 2005, g. 2006, h. 2007, i. 2008, j. 2009, k. 2010, l. 2011, m. 2013, n. 2014, o. 2015, p. 2016, q. 2017, r. 2018, s. 2019, t. 2020, u. 2021, v. 2022, w. 2023, x. 2024

The AAR was estimated for each target year using NDSI-derived snow cover maps (Table 4.4 and Fig. 4.6). These remote sensing-based AAR values were compared with calibrated/estimated AAR values derived from field measurements and modelling studies, where available, to assess consistency and reliability. In 2001 and 2002, only remote-sensing-based AAR values were available, estimated at approximately 0.61 and 0.65, respectively. From 2003 onward, years with both remote-sensing and field data allowed for direct comparison. The agreement was generally strong; for instance, in 2003, the estimated AAR was 0.34, closely matching the observed 0.33. Similarly, 2005—a year characterized by a positive mass balance—showed a high AAR of 0.72 (calibrated value ~0.67), consistent with a favourable accumulation season. In some years, slight discrepancies were observed, such as in 2004, where the estimated AAR (0.39) slightly overestimated the field-derived value (0.32), possibly due to residual late-season snow on the ablation zone. For equilibrium years such as 2009 and 2010, both estimated and observed AARs ranged around 0.63–0.65, indicating near balance. Negative balance years like 2013 and 2018 showed low AARs of 0.42 and 0.33 (observed: 0.34 and 0.30, respectively), reflecting limited accumulation area. In extreme years, such as 2022, the AAR dropped to 0.23 (observed 0.19), suggesting nearly complete loss of the accumulation zone by the end of summer. The long-term average AAR for the 2000–2024 period was approximately 0.50, with notable variability from a minimum of ~0.23 in 2022 to a maximum of ~0.72 in 2005. A downward trend is evident over time: early 2000s often recorded AARs above 0.6, whereas many years in the 2010 ranged between 0.4 and 0.5, and several recent years show values below 0.4. This trend indicates a shift in glacier equilibrium, with the glacier failing to maintain a sufficient accumulation area relative to the expanding ablation zone, leading to sustained mass loss. Climatic correlations support this interpretation. High AAR values corresponded with winters or summers characterized by enhanced snowfall or reduced melt, as in 2005, which followed a snow-rich winter (Wagnon et al., 2007). In contrast, very low AARs such as in 2022 align with reports of anomalously warm conditions

and potentially reduced precipitation, likely contributing to excessive melt and minimal snow retention. These results demonstrate that the AAR method captures interannual climate signals and serves as a useful proxy for glacier mass balance variability.

Table 4.4 AAR Comparison of calibrated and remote sensing derived threshold of Chhota Shigri Glacier

Year/Date	Supervised NDSI Threshold	RS Based AAR	AAR Calibrated/Observed
2000	0.8	0.56	No-Data
2001	0.73	0.61	No-Data
2002	0.84	0.65	No-Data
2003	0.78	0.34	0.33
2004	0.85	0.39	0.32
2005	0.41	0.72	0.67
2006	0.82	0.37	0.32
2007	0.81	0.46	0.36
2008	0.8	0.43	0.40
2009	0.41	0.63	0.63
2010	0.7	0.65	0.65
2011	0.65	0.56	0.50
2012	No-Data	No-Data	0.44
2013	0.75	0.42	0.34
2014	0.82	0.54	0.53
2015	0.85	0.58	0.50
2016	0.85	0.39	0.33
2017	0.9	0.41	0.31
2018	0.83	0.33	0.30
2019	0.83	0.65	0.64
2020	0.91	0.42	0.35
2021	0.83	0.59	0.51
2022	0.87	0.23	0.19
2023	0.8	0.57	0.56
2024	0.85	0.5	No-Data

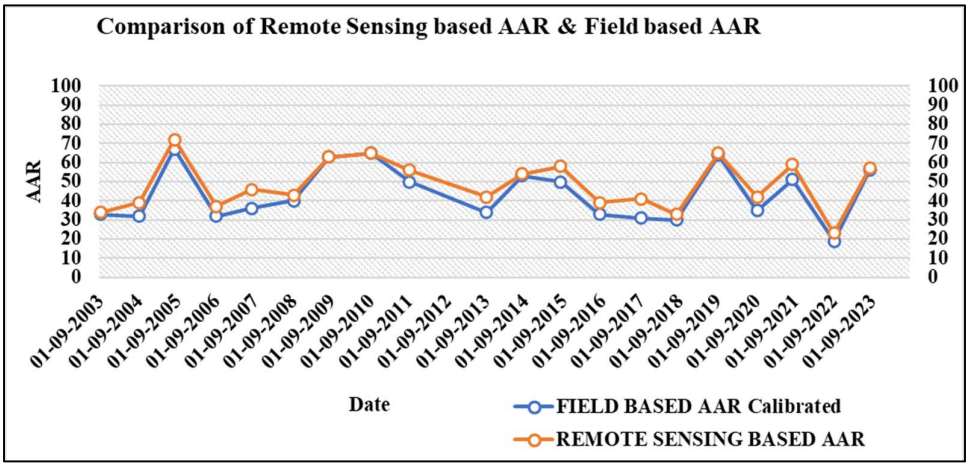

Fig. 4.6 Chart showing the comparison between RS based AAR and Field Calibrated AAR

4.3.1.3 Mass Balance Inference from AAR:

A polynomial regression model was established to correlate the remotely sensed Accumulation Area Ratio (AAR) with glacier mass balance (Fig. 4.7 and Table 4.5), using a calibration period spanning 2003 to 2019. The fitted second-order polynomial equation, derived from 16 years of data, yielded the Mass Balance (MB) equation (Eq. 6):

$$\mathbf{MB = -3.6982AAR^2 + 8.4208AAR - 3.5611} \qquad \text{Eq. 6}$$

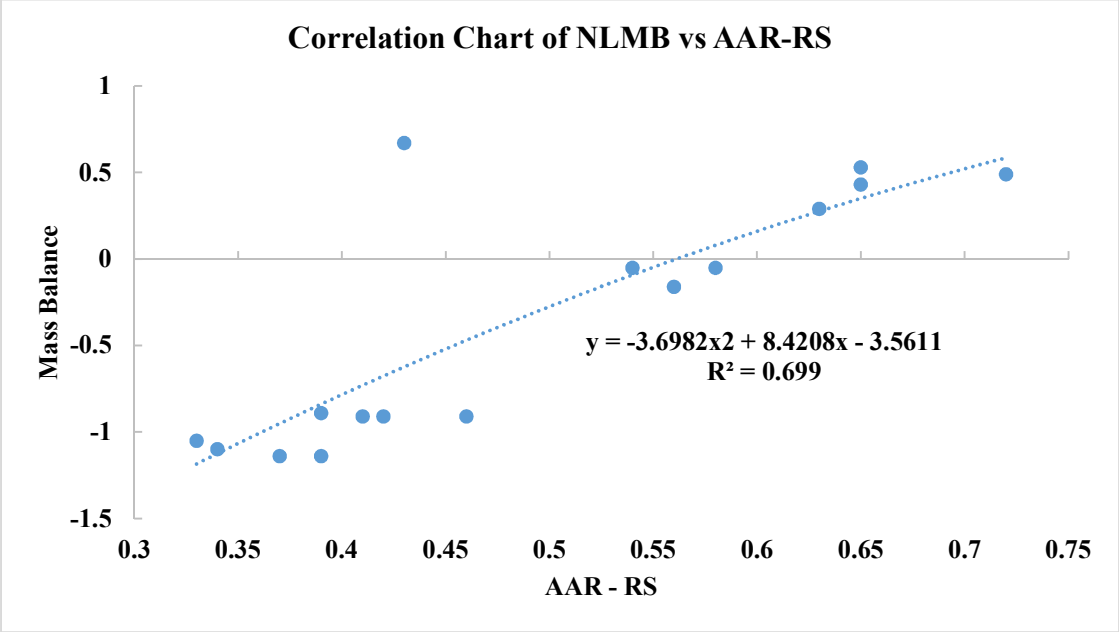

Fig. 4.7 The correlation between NLMB and AAR-RS

This model produced a coefficient of determination (R^2) of 0.699, indicating a moderate-to-strong correlation between AAR and annual mass balance. During the calibration period, mass balance estimates derived from the AAR closely followed the non-linear calibrated values. For example, in 2003 (AAR = 0.34), the calibrated mass balance was –1.10 m w.e., while the AAR-derived value was –1.13 m w.e.; in 2005, a high AAR of 0.72 yielded a positive mass balance of 0.58 m w.e. compared to the calibrated 0.49 m w.e.; and in 2010, both calibrated and remote sensing estimates remained consistent at 0.43 and 0.35 m w.e., respectively.

Table 4.4 The comparison of observed MB vs remote sensing-based MB (Cal/Val)

S. No.	Date		RS Based AAR	Remote sensing-based MB	Non-linear calibrated MB (NLMB)	MB Traditional
1	28-08-2000	Estimation (2000-2002)	0.56	-0.01	NA	NA
2	24-09-2001		0.61	0.2	NA	NA
3	10-05-2002		0.65	0.35	NA	NA
4	22-09-2003	Calibration (2003-2019)	0.34	-1.13	-1.1	-1.34
5	08-09-2004		0.39	-0.84	-1.14	-1.14
6	26-08-2005		0.72	0.58	0.49	0.24
7	30-09-2006		0.37	-0.95	-1.14	-1.33
8	16-08-2007		0.46	-0.47	-0.91	-0.9
9	03-09-2008		0.43	-0.62	0.67	-0.84
10	21-08-2009		0.63	0.28	0.29	0.22
11	09-09-2010		0.65	0.35	0.43	0.42
12	20-09-2011		0.56	-0.01	-0.16	0.17
13			No-Data	-	-0.42	-0.36
14	17-09-2013		0.42	-0.68	-0.91	-0.66
15	27-08-2014		0.54	-0.09	-0.05	0.02
16	30-08-2015		0.58	0.08	-0.05	-0.48
17	16-08-2016		0.39	-0.84	-0.89	-1.18
18	04-09-2017		0.41	-0.73	-0.91	-0.62
19	22-08-2018		0.33	-1.18	-1.05	-0.73
20	10-09-2019		0.65	0.35	0.53	0.21
21	12-09-2020	Validation (2020-2023)	0.42	-0.68	-0.71	-0.26
22	30-08-2021		0.59	0.12	0.04	-1.49
23	02-09-2022		0.23	-1.82	-1.71	-2
24	20-08-2023		0.57	0.04	0.21	-0.22
25	22-08-2024	Estimation	0.5	-0.28	No-Data	

The validation period from 2020 to 2023 further confirmed the model's applicability. For instance, in 2022, the AAR was 0.23, resulting in an estimated mass balance of –1.82 m w.e., which aligned closely with the modeled value of –1.71 m w.e. Similarly, in 2020 (AAR = 0.42), both estimates indicated significant mass loss: –0.71 m w.e. (model) and –0.68 m w.e. (remote sensing). Slight deviations occurred in some years, such as 2008, where the AAR-based estimate suggested a negative balance (–0.62 m w.e.), despite the model indicating a positive balance (0.67 m w.e.), possibly due to snowline misclassification or seasonal snow presence during image acquisition. For years without in situ or modelled mass balance data (e.g., 2000, 2001, 2002 and 2024), mass balance values were directly estimated using the polynomial equation. In 2000, 2001 and 2002, AARs of 0.56, 0.61 and 0.65 resulted in estimated mass balances of -0.01, 0.20 and 0.35 m w.e., respectively, while in 2024, with an AAR of 0.50, the derived mass balance was –0.28 m w.e.

Over the entire 2000–2024 period, the glacier exhibited substantial interannual variability in AAR and corresponding mass balance, ranging from a maximum AAR of 0.72 (2005, strongly positive balance) to a minimum of 0.23 (2022, extreme mass loss). The average AAR across the time series was approximately 0.50, with an associated mean annual mass balance of around –0.30 to –0.35 m w.e. a^{-1}, indicating sustained long-term glacier mass loss.

The cumulative mass loss over the 25-year period is estimated at approximately –7.9 to –8.1 m w.e., equivalent to a significant reduction in glacier volume. The long-term trend indicates a glacier in persistent disequilibrium, with increasingly negative balances in recent years driven by high ELAs and limited accumulation area. Despite some scatter in the fit, particularly at extreme AAR values, the polynomial model demonstrates robust predictive capability and confirms the sensitivity of the AAR method to climatic forcing and glacier response.

An analysis of glacier mass balance values between 2003 and 2019, derived from both remote sensing-based methods and non-linear calibrated mass balance, shows a strong correspondence in overall trends, despite some year-to-year differences. During the early part of this period, both datasets indicate negative mass balance conditions, such as in 2003 and 2004, where remote sensing estimates were –1.13 m w.e. and –0.84 m w.e., while traditional methods reported –1.34 m w.e. and –1.14 m w.e., respectively. A notable positive balance occurred in 2005, with remote sensing estimating 0.58 m w.e. and traditional methods indicating 0.24 m w.e., reflecting a favourable accumulation year. In contrast, 2006 and 2007 showed renewed mass loss in both records. The agreement continued in years like 2008 and 2009, where moderate balances were recorded, and in 2010 and 2011, which showed near-equilibrium or slightly positive values. The period from 2013 to 2015 revealed some variation: remote sensing values ranged from –0.68 m w.e. to –0.09 m w.e., while traditional methods reported –0.66 m w.e. to 0.02 m w.e., showing a similar trajectory. Mass loss intensified again in 2016 and 2018, with both methods capturing substantial negative balances. The cumulative mass balance for the period 2001-2024 (except 2012) was estimated to be -7.97 m w.e.

A comparative assessment of glacier mass balance for the period 2003–2023, based on remote sensing-derived AAR estimates and traditional glaciological observations, reveals strong consistency in both annual variability and overall trends. Years with substantial mass loss such as 2003 (–1.13 vs –1.34 m w.e.), 2006 (–0.95 vs –1.33 m w.e.), 2016 (–0.84 vs –1.18 m w.e.), and 2022 (–1.82 vs –2.00 m w.e.) show close agreement across both methods. Positive or near-equilibrium years like 2005 (0.58 vs 0.24 m w.e.), 2010 (0.35 vs 0.42 m w.e.), and 2019 (0.35 vs 0.21 m w.e.) were also reliably captured. While occasional discrepancies occurred - such as in 2015 (0.08 vs –0.48 m w.e.) and 2021 (0.12 vs –1.49 m w.e.) - these are likely due to differences in image timing, localized events, or sensor limitations. Despite some differences in exact magnitudes - likely due to factors such as transient snow, image timing, and debris cover - the remote sensing approach consistently reflects the interannual variability observed in traditional measurements. This reinforces its utility for long-term glacier monitoring in data-scarce regions like the Himalaya.

4.3.1.4 Uncertainties and Discussion (AAR):

The reliability of AAR-based mass balance estimates is closely tied to the accurate delineation of the annual snowline. Although high-quality satellite imagery was used and field observations were referenced where available, some uncertainties persist. For example, no suitable image was obtained for 2012 due to persistent cloud cover during the monsoon season, resulting in the exclusion of that year from the analysis. The methodology assumes that the late-summer snowline corresponds to the glacier's annual ELA; however, unseasonal weather events—such as early snowfall after the end of the ablation season but before image

acquisition—can introduce errors by altering the apparent snowline. Additionally, the empirical conversion of AAR to mass balance adds another source of uncertainty. Importantly, mass balance estimation from AAR was conducted using a second-order polynomial regression, rather than a linear fit, to better represent the nonlinear relationship between AAR and mass balance. This approach is particularly valuable in capturing extreme conditions at both high and low AAR values, which linear models may misrepresent. Looking ahead, continued negative mass balances are expected to accelerate terminus retreat, especially as the glacier moves into higher elevation zones that may no longer provide sufficient mass gain. Although the rate of terminus retreat has slowed in recent years, likely due to the glacier reaching these higher elevations, ongoing warming could result in continued mass loss even in these zones, driving further retreat and degradation of the glacier.

4.3.1.5 Conclusion for the AAR results

Based on the remote sensing-derived Accumulation Area Ratio (AAR) values, Chhota Shigri Glacier has experienced a notable decline in accumulation conditions over the past two decades. In the early 2000s, AAR values were relatively high — 0.61 in 2000 and 0.65 in 2001 — indicating near-equilibrium or slightly positive mass balance conditions. However, by 2003, AAR dropped sharply to 0.34, and although there were brief recoveries in years such as 2005 (0.72) and 2010 (0.65), the overall trend has been downward. From 2015 onward, AAR values frequently fell below 0.4, with several years — such as 2016 (0.39), 2017 (0.41), 2018 (0.33), and 2022 (0.23) — indicating severe mass loss and minimal accumulation areas. The year 2022, in particular, marks one of the lowest AARs on record, suggesting widespread ablation with almost no retained snow cover. Although a few recent years like 2019 (0.65) and 2023 (0.57) show short-term recovery, the decadal pattern clearly reflects a shift toward increasingly negative glacier mass balance. This trend supports the conclusion that the glacier is undergoing persistent disequilibrium, with insufficient accumulation to counterbalance annual melt, particularly during the post-2015 period.

4.3.2 Geodetic Method Results

4.3.2.1 Elevation Change Distribution

The differencing of DEMs over Chhota Shigri Glacier reveals a heterogeneous pattern of ice thickness change from 2000 to 2024. The glacier has thinned across almost its entire length, with the magnitude of thinning generally increasing toward lower elevations. The greatest thickness losses were observed near the glacier terminus and along the lower tongue, where down wasting of >40 m locally occurred (consistent with the terminus retreat and stagnation seen). Notably, a significant morphological change was captured: the western tributary's detachment in 2012. Up to 2010, that tributary (feeding from the west) was part of the glacier; by 2020, it had disconnected. This event is clearly visible in high-res imagery (Farooq Azam et al., 2024) and our elevation change maps confirm it – essentially a portion of the glacier no longer contributing mass after 2012. Overall, the spatial pattern is one of

pronounced mass loss in the lower glacier and relative stability (but still slight loss) in the upper glacier.

4.3.2.2 Glacier Mass Balance for Multi-annual Intervals during 2000–2024

The geodetic mass balance estimates from 2000 to 2024 reveal a consistent negative trend (Table 6), indicative of sustained glacier mass loss. Over the first interval (2000–2009), the glacier experienced a total loss of –3.4 ± 1.44 m w.e., translating to a moderate annual rate of –0.37 ± 0.16 m w.e. a^{-1}. For the extended period of 2000–2015, the cumulative loss increased to –4.36 ± 0.31 m w.e., although the annual rate slightly declined to –0.29 ± 0.02 m w.e. a^{-1}. This suggests that the 2010–2015 sub-period may have had relatively better mass balance years, supported by near-equilibrium conditions observed in 2010. Between 2009 and 2015, a total loss of –1.88 ± 0.44 m w.e. was recorded, with an annual rate of –0.31 ± 0.07 m w.e. a^{-1}, comparable to the early 2000s, indicating a phase of moderate but consistent loss.

A marked shift occurred during 2015–2020, with a sharp increase in mass loss amounting to –4.49 ± 0.54 m w.e. in just five years, corresponding to an accelerated rate of –0.89 ± 0.11 m w.e. a^{-1}—the highest among all observed intervals. This intensified thinning phase is corroborated by concurrent AAR-based results and likely reflects the influence of successive low-accumulation and high-ablation years during this period. From 2020 to 2024, glacier mass loss continued, totaling –2.83 ± 0.95 m w.e., with a slightly lower annual rate of –0.70 ± 0.23 m w.e. a^{-1}. Although still significant, this suggests a minor reduction in ice loss intensity compared to the late 2010s. The larger uncertainty in this period is attributed to its shorter duration and reliance on the ASTER 2024 DEM, which may not fully capture the melt season of that year.

Table 4.5 Comparison of Mass Balance by different methods

Time Period	Calibrated Non-Linear	Calibrated Glaciological	Geodetic Mass balance (Azam et al., 2024)	Geodetic Mass Balance (This study)	AAR Based Mass Balance (This study)
2000-2015				-4.36 ± 0.31	-2.95 (excluding 2012)
i. **2000-2014**			-4.18 ± 0.38 (2003-2014)		-3.03 (excluding 2012)
ii. **2003–2009**	-2.84 ± 1.35	-5.09		-3.4 ± 1.44 (2000-2009)	-3.15
iii. **2003–2015**	-4.00 ± 2.46	-5.98			-3.5 (excluding 2012)
2009–2015	-0.87 ± 1.11	-0.67		-1.88 ± 0.44	-0.07 (excluding 2012)
2015–2020	-3.08 ± 0.8	-3.06	-3.08 ± 0.51 (2014-2020)	-4.49 ± 0.54	-3.00
2020–2024	-2.17 ± 0.87 (2020-2023)	-3.97 (2020-2023)		-2.83 ± 0.95	-2.61
2000–2024	-8.70 ± 3.97 (2020-2023)	-12.27 (2020-2023)		-11.68 ± 1.8*	-7.97

Cumulatively, the glacier lost approximately –11.68 ± 1.80 m w.e. over the 24-year period, with an average annual specific mass balance of –0.69 ± 0.06 m w.e. a^{-1}. A comparison of geodetic and remote sensing-based AAR-derived glacier mass balance estimates across multiple timeframes demonstrates a reasonable level of agreement, reinforcing the reliability of the AAR method. For the period 2000–2015, the geodetic mass balance is estimated at –4.36 ± 0.31 m w.e., while the AAR-based estimate is –2.95 m w.e. (excluding 2012). Sub-period analyses further validate this correlation: between 2000–2014, the AAR method gives –3.03 m w.e., closely matching the geodetic estimate of –3.4 ± 1.44 m w.e. for 2000–2009. For the period 2003–2009, AAR estimates yield –3.15 m w.e., while for 2003–2015, it is –3.5 m w.e., again excluding 2012. During 2009–2015, the AAR-derived balance is –1.88 ± 0.44 m w.e., whereas geodetic estimates suggest a significantly lower loss of –0.07 m w.e., indicating possible underrepresentation of short-term changes in remote sensing due to cloud/snow cover or limited image availability. In the period 2015–2020, geodetic and AAR methods show better convergence, with estimates of –4.49 ± 0.54 m w.e. and –3.00 m w.e., respectively. Similarly, from 2020–2024, mass losses of –2.83 ± 0.95 m w.e. (geodetic) and –2.61 m w.e. (AAR) indicate continued negative trends. Over the full period 2000–2024, the cumulative glacier mass loss is estimated at –11.68 ± 1.8 m w.e. geodetically and –7.97 m w.e. using the AAR approach (excluding 2012), confirming that the AAR-based method captures the long-term loss trajectory effectively, with some differences likely due to temporal resolution and classification uncertainties inherent in optical remote sensing.

4.3.2.3 Comparison with Previous Studies

A comparison of glacier mass balance estimates between this study and those reported by Farooq Azam et al. (2024) reveals overall agreement in trends, but also highlights certain differences in magnitude across overlapping periods. For the period 2000–2015, our geodetic mass balance estimate of –4.36 ± 0.31 m w.e. is in close agreement with Azam et al.'s glaciological balance of –4.18 ± 0.38 m w.e. for 2000–2014 (noting that our period includes 2015, a year of significant loss, which may account for the slight additional negative balance). During 2003–2009, Azam et al.'s calibrated nonlinear model reports –2.84 ± 1.35 m w.e., and the glaciological method –5.09 m w.e., both broadly comparable with our geodetic estimate of –3.4 ± 1.44 m w.e. (for 2000–2009), reflecting inter-method variability but similar directional trends.

For the extended period 2003–2015, Azam's nonlinear model estimates a cumulative balance of –4.00 ± 2.46 m w.e., whereas the modelled glaciological balance is –5.98 m w.e., suggesting their glaciological approach may capture more ablation. Our geodetic data, though not explicitly stated for this period, suggest an intermediate loss magnitude, consistent with this range. In the sub-period 2009–2015, our –1.88 ± 0.44 m w.e. estimate is notably more negative than Azam's –0.87 ± 1.11 m w.e. (nonlinear) and –0.67 m w.e. (glaciological), possibly due to differences in spatial coverage, stake placement, or short-term climatic conditions that were under- or overrepresented in the respective methods.

In the period 2015–2020, our geodetic mass balance of –4.49 ± 0.54 m w.e. is significantly more negative than Azam's values (–3.08 ± 0.8 m w.e. nonlinear, –3.06 m w.e.

glaciological, and their own geodetic estimate of –3.08 ± 0.51 m w.e. for 2014–2020). This difference may be attributed to residual radar penetration biases in SRTM or differing treatment of dynamic changes such as tributary detachment, which may have contributed additional loss not captured by stake networks. From 2020 to 2024, our estimate of –2.83 ± 0.95 m w.e. lies between Azam's model-based estimate of –2.17 ± 0.87 m w.e. and their glaciological estimate of –3.97 m w.e., indicating acceptable agreement despite the use of differing input data and time ranges (their estimates span 2020–2023 only).

Over the full glacier mass balance record, 2000–2024, our geodetic cumulative loss is –11.68 ± 1.8 m w.e., while Azam's extrapolated totals suggest –12.27 m w.e. (glaciological) and –8.70 ± 3.97 m w.e. (nonlinear model). The discrepancy of ~3 m w.e. over the 24-year span may reflect compounded minor methodological differences—such as density assumptions (e.g., 850 kg/m³ vs variable firn/ice), radar penetration corrections, or spatial inclusion of disconnected glacier zones. Despite these differences, the convergence in overall trends, especially the pronounced mass loss in 2015–2020, underscores a shared understanding of rapid glacier degradation during recent decades. The close alignment across methods in many periods also validates the robustness of our geodetic workflow and corrections, while reinforcing the importance of multi-method cross-validation in Himalayan glacier mass balance studies.

4.3.2.4 Accuracy and Uncertainty

The reliability of the geodetic results as follows. On stable ground, the elevation difference mean was ~0 (after co-registration) with standard deviation ~5–8 m for ASTER vs SRTM differences. Over the glacier, some of that noise persisted, but averaging over several pixels reduced random error. The largest source of uncertainty is systematic bias: radar penetration in 2000 and any undetected tilt in DEMs. We tried a penetration correction, but if it's off by a couple of meters, that could bias the accumulation area change and thus the total mass by maybe 5–10%. We also looked at ASTER 2009 vs 2020 Pléiades difference (to see 2009–2020) and ASTER 2015 vs 2020 – these confirmed the major mass loss occurred post-2015. If any DEM had a seasonal bias (e.g., one DEM captured in late summer when snow was gone vs another in mid-summer with snow), it could affect local changes. The 2015 ASTER was from around October (minimal snow), 2020 Pléiades from September (minimal snow), 2009 ASTER from summer (some patches possible). In view of this, we assume the impact of seasonal snow to be small relative to the tens of meters of long-term change over multiple years. Uncertainty in density (we used 850) adds about ±7% uncertainty. Taking all these into account, we estimate the error on the 25-year mass change is on the order of ±15%. The trends discussed (increase in loss rate, etc.) are well above these uncertainty levels and are robust.

It is also instructive to consider how these methods complement each other. The AAR method is less data-intensive – just needing optical images – and can provide annual estimates, but it needs calibration and cannot directly measure the volume loss. The geodetic method directly measures volume change and does not need calibration with mass balance, but it gives a multi-year average and requires high-quality DEMs which might only come every few years. In our study, we effectively used the geodetic results to validate the cumulative outcome of the

annual AAR method. The AAR method, in turn, provided insight into the timing and cause of changes (for instance, identifying which specific years drove the mass loss and linking those to high ELAs). The combination is powerful: for example, geodetic method showed that 2015–2020 was the worst mass loss period; AAR pinpointed that within 2015–20, 2018 and 2019 had extraordinarily low AAR (and perhaps 2016 too), indicating those specific summers were extremely warm/dry.

The implications of these findings are significant for water resources. A continuously negative mass balance means Chhota Shigri is contributing extra meltwater runoff to River Chandra that becomes the Chenab downstream in the short term, but this runoff is unsustainable – and eventually, as the glacier ice reserve diminishes, the contribution will decrease in a downward spiral. The period of accelerated loss may correspond to increased summer flows in the Chenab basin, raising concerns for glacier lake outburst floods or hydrological shifts. The retreat and thinning also mean the glacier's geometry is changing, which can affect its flow dynamics (a thinner glacier has less driving stress to flow, possibly leading to reduced velocity and even more stagnation in the tongue). Indeed, the formation of a proglacial moraine-dammed lake is a possibility if rapid retreat continues (though none is reported yet for CSG).

To sum up the geodetic results: From 2000 to 2024, Chhota Shigri Glacier lost nearly 12 meters water equivalent of ice, with an acceleration around 2015–2020 where annual losses approached 0.9 m w.e. This is consistent with field measurements and AAR analyses, and highlights the glacier's response to recent climatic warming. The slight moderation in rate of mass loss after 2020 does not indicate recovery, merely a lesser negative but still highly negative balance. Unless there are a series of unusually positive mass balance years (which would require colder/wetter conditions), the glacier will continue to shrink. Our combined evidence strongly suggests that Chhota Shigri (and by extension similar glaciers in the region) are undergoing a sustained decline that has few signs of stopping under current climate trajectories.

CHAPTER 5

SUMMARY AND CONCLUSIONS

5.1 Overview

Himalayan Cryosphere is a critical resource that caters to the sustainable development goals of the nation by way of being the most reliable regional water storage that serves when most needed, ie. in the summer season. Western Himalayan Region is mainly fed by the Indus River System comprising of the Indus, Jhelum, Chenab, Ravi, Sutlej and Beas rivers. These rivers are significantly dependant on snow and glacier melt to support the lives and livelihoods of the human population as well as the diverse ecosystems that are sustained by them. For example, River Chenab is credited to have about fifty percent of its flows sourced from snow and glacier melt. With the warming climate affecting this store house of solid water negatively, it is imperative that we gain sufficient understanding of the dynamic nature of this critical resource and various repercussions arising from its depletion, so that adaptation and mitigation measures can be in place as and when required. Considering the vast areas, rugged terrain involved, and the advances in satellite remote sensing techniques in the recent decades, it is prudent to have reliable assessments of the decadal, interannual and seasonal changes in snow cover area at sub-basin scale and develop proxies for assessing the mass changes of glacier at annual and decadal time scales. Simultaneous assessments of climate change at the sub-basin scale makes sense to have an understanding of how climate-cryosphere feedbacks are playing out in diverse hydro-climatic regimes.

In view of the above, and by way of developing capabilities at NIH-WHRC to address these needs, a study was formulated with the following objectives:

a) Investigation of snow cover changes and cryosphere-climate linkages in Upper Chenab River Basin (UCRB)

b) Estimation of specific glacier mass balance in UCRB

A multi-faceted methodology was employed to investigate snow cover dynamics in the UCRB using remote sensing, geospatial analysis, and climatological data. A total of 939 MODIS MOD10A2 eight-day composite snow cover products (2000–2020) from the TERRA satellite were analyzed at 500 m spatial resolution, capturing maximum snow extent defined as areas with snow presence during any day of the eight-day interval. Topographic stratification of the basin was performed using SRTM 90 m DEM-derived elevation, slope, and aspect maps to assess snow distribution patterns. For climate trend analysis, ERA5-Land hourly datasets (1950–2021) of temperature and precipitation at 9 km resolution were processed. Trend detection was conducted using the Modified Mann-Kendall test and Thiel-Sen's slope estimator across five overlapping 30-year climatic windows (1951–1980, . . . 1991–2020) and the full 72-year period (1950-2021), with anomalies calculated relative to the 1961–1990 baseline per WMO guidelines. Positive Degree Days (PDD > 2°C) were computed as a melt indicator, with their spatiotemporal trends analyzed to quantify warming impacts on

cryospheric processes. The comprehensive methodology integrated satellite-derived snow cover patterns with long-term climate trends, enabling robust assessment of snow cover-climate interactions while accounting for topographic controls. All statistical analyses were performed at 5% significance level using established computational frameworks, ensuring methodological rigor in detecting climate-driven cryosphere changes in the UCRB. The overlapping multiple climate window approach facilitated identification of both gradual trends and abrupt shifts in snow cover dynamics under changing climatic conditions.

Two distinct methodologies were employed to estimate the mass balance of Chhota Shigri Glacier, a globally recognized representative glacier in UCRB from 2000 to 2024: (1) a remote sensing approach based on Accumulation Area Ratio (AAR) and related Equilibrium Line Altitude (ELA) analyses, and (2) a Geodetic approach based on DEM differencing. Satellite imagery and DEM datasets were processed using a combination of Google Earth Engine (for image processing), GIS software, and statistical analysis tools. For AAR method, glacier accumulation areas were delineated on multi-temporal optical images, the accumulation area ratio computed and the non-linear relationship between AAR and mass balance was captured using a calibration model-derived polynomial equation. The geodetic method involved obtaining multiple DEMs, aligning them in a common reference frame, subtracting elevations to get thickness changes, and converting to mass change, which were also employed to verify AAR based annual mass balances.

5.2 Conclusions

The following specific conclusions were derived based on the analyses carried out during the study:

5.2.1 Snow Cover Extent and Snowfall

A strong correlation between elevation and snow cover extent, with higher elevations experiencing more persistent and extensive snow coverage was observed during the study period, crucial for understanding snow accumulation and melt patterns influencing hydrological processes in the UCRB. While gentler slopes tend to retain more snow cover, variations exist across steeper terrain due to complex interactions between topography, solar radiation, and wind redistribution. The contrast in snow retention highlights the influence of aspect on snowmelt dynamics, with South-facing slopes experiencing more pronounced snow loss due to greater exposure to solar radiation, while North-facing slopes retain snow more effectively. The findings underscore the importance of elevation, slope and aspect-based analysis in understanding snow dynamics, which has implications for hydrological modeling and water resource management in the region.

Even though UCRB is a snow dominated basin, interannual variations were evident, mostly driven by variations in winter precipitation, with average annual snow cover reaching close to 90% for hydrological years 2004–2005, 2009–2010, and 2018–2019, while 2016–2017 recorded the lowest average snow extent (74%), reflecting potential anomalies in snowfall patterns. The trend analysis of annual snowfall across different climatic windows highlighted the complex nature of climate dynamics in the region. Although the trends were not found to

be statistically significant in most cases, the overall linear direction of the trend remained negative over the last two climatic windows, covering the past 40 years since 1981. This persistent declining trend raises concerns about the long-term sustainability of snowfall in the region and its potential implications for hydrological and ecological systems. Overall, snowfall trends remained largely negative in the last three climatic windows, covering the past 50 years since 1971, indicating a persistent decline in winter snowfall over time.

5.2.2 Temperature

The temperature analysis highlights the seasonal contrast in temperature variations, with persistent cold conditions in winter and a gradual warming trend in summer. This shifting thermal regime is likely to influence glacier dynamics, snow accumulation, and overall water balance in the UCRB, necessitating continuous monitoring and climate impact assessments. Despite the climatic variability observed among different climatic windows, the underlying persistent increase in summer temperature is expected to accelerate snowmelt and alter the hydrological regime, potentially impacting water availability and runoff patterns in the region. The strong correlation between rising summer temperatures and decreasing snowfall suggests that temperature-driven changes in the cryosphere are playing a critical role in altering the regional hydroclimatic balance. These findings underscore the necessity for continued monitoring and modeling efforts to understand the long-term implications of warming trends on the basin's hydrological processes.

The long-term trend from 1950 to 2020 exhibited an overall increase in PDD, although only a few grid points showed statistically significant positive trends. The long-term variability in PDD anomalies exhibits substantial interannual fluctuations, with alternating periods of positive and negative anomalies before 2000. This suggests episodic warming and cooling phases. However, post-2000, a notable shift towards persistent and intensified warming is evident, marked by consistently positive anomalies that indicate a sustained increase in the number of warmer days conducive to snow and ice melt. The increase in PDD anomalies post-2000 has profound implications for glacier health, streamflow seasonality, and water availability. Higher PDD counts correlate with enhanced glacier mass loss and an earlier onset of snowmelt, potentially leading to early summer runoff but reduced water availability in late summer and autumn. These findings of PDD analysis align with the earlier discussions on temperature and snowfall trends, reinforcing the evidence of intensified warming post-2000. The increasing PDD anomalies, particularly in recent decades, highlight enhanced snowmelt conditions, which have critical implications for the hydrological balance of the Chandrabhaga River Basin.

5.2.3 Glacier Mass Balance by modified AAR and DEM Differencing

Based on the remote sensing-derived Accumulation Area Ratio (AAR) values, Chhota Shigri Glacier has experienced a notable decline in accumulation conditions over the past two decades. In the early 2000s, AAR values were relatively high — 0.61 in 2000 and 0.65 in 2001 — indicating near-equilibrium or slightly positive mass balance conditions. However, by 2003, AAR dropped sharply to 0.34, and although there were brief recoveries in years such as 2005 (0.72) and 2010 (0.65), the overall trend has been downward. From 2015 onward, AAR values frequently fell below 0.4, with several years — such as 2016 (0.39), 2017 (0.41), 2018 (0.33),

and 2022 (0.23) — indicating severe mass loss and minimal accumulation areas. The year 2022, in particular, marks one of the lowest AARs on record, suggesting widespread ablation with almost no retained snow cover. Although a few recent years like 2019 (0.65) and 2023 (0.57) show short-term recovery, the decadal pattern clearly reflects a shift toward increasingly negative glacier mass balance. This trend supports the conclusion that the glacier is undergoing persistent disequilibrium, with insufficient accumulation to counterbalance annual melt, particularly during the post-2015 period.

Chhota Shigri Glacier has undergone significant mass loss over the past 25 years, as evidenced by remote sensing-based AAR analysis and geodetic DEM differencing. The AAR method revealed a declining accumulation area ratio and a rising equilibrium line altitude since 2000, indicating increasingly negative mass balance conditions. Many post-2010 years recorded AAR values well below the ~0.5–0.6 threshold for balance, consistent with warmer summers and reduced snowfall. Geodetic analysis independently confirmed this trend, estimating an average mass loss of approximately –0.7 m w.e. a^{-1} from 2000 to 2024. This long-term loss corresponds with ~0.57 km² of area reduction (~3.6%), ~577 m of terminus retreat, and 20–30 m of surface thinning in the ablation zone. Both methods consistently identified 2015–2020 as a period of accelerated loss, driven by climatic anomalies, while 2021–2024 showed slightly reduced but still strongly negative balances.

Comparative analysis demonstrated strong agreement between the AAR and geodetic results, with discrepancies falling within uncertainty margins. Temporal resolution from AAR analysis highlighted interannual climate influences, while geodetic data provided spatial context, identifying the lower glacier and detached tributary as key contributors to volume loss. These findings align with broader Himalayan trends of glacier retreat under warming conditions (Bolch et al., 2012; Zemp et al., 2019). Thud continued monitoring—through field measurements, remote sensing, or integrated approaches—is essential.

This study reinforces the utility of combining AAR and geodetic methods for glacier mass balance estimation. While AAR offers annual insights, periodic geodetic surveys provide a robust long-term benchmark. In data-sparse regions, calibrated AAR analysis can extend mass balance series, with geodetic validation enhancing reliability. Chhota Shigri Glacier remains a critical benchmark for the western Himalaya, and multi-method assessments such as this are vital for understanding glacier response to climate change and informing hydrological forecasting in glacier-fed basins.

REFERENCES

Aggarwal, S., Rai, S. C., Thakur, P. K., & Emmer, A. (2017). Inventory and recently increasing GLOF susceptibility of glacial lakes in Sikkim, Eastern Himalaya. Geomorphology, 295, 39–54. https://doi.org/10.1016/j.geomorph.2017.06.014

Aggarwal, S.P., Thakur, P.K., Nikam, B.R., & Garg, V. (2014). Integrated approach for snowmelt run-off estimation using temperature index model, remote sensing and GIS. Current Science, 106(3), 397–407.

Azam, M.F., Wagnon, P., Ramanathan, Al., Vincent, C., Sharma, P., Arnaud, Y., Linda, A., Pottakkal, J. G., Chevallier, P., Singh, V. B., Berthier, E. (2012) From balance to imbalance: a shift in the dynamic behaviour of Chhota Shigri glacier, western Himalaya, India. Journal of Glaciology 58(208), 315–324. doi: 10.3189/2012JoG11J123.

Azam, M. F., Ramanathan, A. L., Wagnon, P., Vincent, C., Linda, A., Berthier, E., Sharma, P., Mandal, A., Angchuk, T., Singh, V. B., & Pottakkal, J. G. (2016). Meteorological conditions, seasonal and annual mass balances of Chhota Shigri Glacier, western Himalaya, India. Annals of Glaciology, 57(71), 328–338. https://doi.org/10.3189/2016AoG71A570

Azam, M. F., Vincent, C., Srivastava, S., Berthier, E., Wagnon, P., Kaushik, H., Hussain, A., Kumar Munda, M., & Mandal, A. (2024). Reanalysis of the longest mass balance series in Himalaya using nonlinear model: Chhota 1 Shigri Glacier (India) 2. April, 1–35. https://doi.org/10.5194/egusphere-2024-644

Azam, M. F., Wagnon, P., Berthier, E., Vincent, C., Fujita, K., & Kargel, J. S. (2018). Review of the status and mass changes of Himalayan-Karakoram glaciers. Journal of Glaciology, 64(243), 61–74. https://doi.org/10.1017/jog.2017.86

Azam, M. F., Wagnon, P., Vincent, C., Ramanathan, AL., Kumar, N., Srivastava, S., Pottakkal, J.G., Chevallier, P. (2019) Snow and Ice melt contributions in a highly glacierized catchment of Chhota Shigri Glacier (India) over the last five decades, Journal of Hydrology. https://doi.org/10.1016/j.jhydrol. 2019.04.075

Azam, M. F., Vincent, C., Srivastava, Smriti, Berthier, E., Wagnon, P., Kaushik, H., Hussain, A., Munda, M.K., Mandal, A. and Alagappan R. (2024) Reanalysis of the longest mass balance series in Himalaya using nonlinear model: Chhota Shigri Glacier (India)

Berthier, E., Arnaud, Y., Kumar, R., Ahmad, S., Wagnon, P., & Chevallier, P. (2007). Remote sensing estimates of glacier mass balances in the Himachal Pradesh (Western Himalaya, India). Remote Sensing of Environment, 108(3), 327–338. https://doi.org/10.1016/j.rse.2006.11.017

Baud, A., Gaetani, M., Garzanti, E., Fois, E., Nicora, A., & Tintori, A. (1984). Geological observations in southeastern Zanskar and adjacent Lahul area (northwestern Himalaya). Eclogae Geologicae Helvetiae, 77, 171–197.

Berthier, E., Lebreton, J., Fontannaz, D., Hosford, S., Belart, J. M. C., Brun, F., Andreassen, L. M., Menounos, B., & Blondel, C. (2024). The Pléiades Glacier Observatory: High-

resolution digital elevation models and ortho-imagery to monitor glacier change. Cryosphere, 18(12), 5551–5571. https://doi.org/10.5194/tc-18-5551-2024

Bishop, M.P., Barry, R.G., Bush, A.B.G., Copland, L., Dwyer, J.L., Fountain, A.G., Haeberli, W., Hall, D.K., Kääb, A., Kargel, J.S.(2004a): Global land-ice measurements from space (GLIMS): Remote sensing and GIS investigations of the Earth's cryosphere. Geocarto International. Volume.19 No.2, pp. 57–84.

Bisht, D.S., Chatterjee, C., Raghuwanshi, N.S., & Sridhar, V. (2017). An analysis of precipitation climatology over Indian urban agglomeration. Theoretical and Applied Climatology, 133, 421–436. https://doi.org/10.1007/s00704-017-2200-z

Bolch, T., Kulkarni, A., Kääb, A., Huggel, C., Paul, F., Cogley, J. G., Frey, H., Kargel, J. S., Fujita, K., Scheel, M., Bajracharya, S., & Stoffel, M. (2012). The state and fate of himalayan glaciers. Science, 336(6079), 310–314. https://doi.org/10.1126/science.1215828

Bookhagen, B., Thiede, R.C., & Strecker, M.R. (2005). Abnormal monsoon years and their control on erosion and sediment flux in the high, arid northwest Himalaya. Earth and Planetary Science Letters, 231, 131–146.

Brun, F., Berthier, E., Wagnon, P., Kääb, A., & Treichler, D. (2017). A spatially resolved estimate of High Mountain Asia glacier mass balances from 2000 to 2016. Nature Geoscience, 10(9), 668–673. https://doi.org/10.1038/ngeo2999

Chahal, P., Kumar, A., Sharma, C.P., et al. (2019). Late Pleistocene history of aggradation and incision, provenance and channel connectivity of the Zanskar River, NW Himalaya. Global and Planetary Change, 178, 110–128.

Cogley, J. G. (2009). Geodetic and direct mass-balance measurements: Comparison and joint analysis. Annals of Glaciology, 50(50), 96–100. https://doi.org/10.3189/172756409787769744

Das, S., Sharma, M. C., & Murari, M. K. (2022). Spatially heterogeneous glacier elevation change in the Jankar Chhu Watershed, Lahaul Himalaya, India derived using ASTER DEMs. Geocarto International, 37(27), 17799–17825. https://doi.org/10.1080/10106049.2022.2136254

Dharpure, J.K., Patel, A., Goswami, A., et al. (2020). Spatiotemporal snow cover characterization and its linkage with climate change over the Chenab river basin, western Himalayas. GIScience & Remote Sensing, 00, 1–25.

Dixit, A., Goswami, A., Jain, S. & Das, D. (2024) Assessing snow cover patterns in the Indus-Ganga-Brahmaputra River Basins of the Hindu Kush Himalayas using snow persistence and snow line as metrics. Environmental Challenges, 14, 100834. https://doi.org/10.1016/j.envc.2023.100834

Engelhardt, M., Ramanathan, A., Eidhammer, T., Kumar, P., Landgren, O., Mandal, A., & Rasmussen, R. (2017). Modelling 60 years of glacier mass balance and runoff for

Chhota Shigri Glacier, Western Himalaya, Northern India. Journal of Glaciology, 63(240), 618–628. https://doi.org/10.1017/jog.2017.29

Gardelle, J., Berthier, E., Arnaud, Y., & Kääb, A. (2013). Region-wide glacier mass balances over the Pamir-Karakoram-Himalaya during 1999–2011. Cryosphere, 7(4), 1263–1286. https://doi.org/10.5194/tc-7-1263-2013

Garg, V., Kudekar, A. R., Thakur, P. K., Nikam, B. R., Aggarwal, S. P., & Chauhan, P. (2021). Glacier Change Studies under Changing Climate Using Geospatial Tools and Techniques. Journal of the Indian Society of Remote Sensing, 49(10), 2387–2406. https://doi.org/10.1007/s12524-021-01388-5

Gergan, J. T. & Thayyen, R. J. (2010) Role of glaciers in watershed hydrology: a preliminary study of a "Himalayan catchment".

Girod, L., Nuth, C., Kääb, A., McNabb, R., & Galland, O. (2017). MMASTER: Improved ASTER DEMs for elevation change monitoring. Remote Sensing, 9(7). https://doi.org/10.3390/rs9070704

Gurung, D. R., Kulkarni, A. V., Giriraj, A., Aung, K. S., Shrestha, B., and Srinivasan, J. (2011) Changes in seasonal snow cover in Hindu Kush-Himalayan region, The Cryosphere Discuss., 5, 755–777, https://doi.org/10.5194/tcd-5-755-2011.

Hall, D.K., Riggs, G.A., & Salomonson, V.V. (1995). Development of methods for mapping global snow cover using moderate resolution imaging spectroradiometer data. Remote Sensing of Environment, 54, 127–140.

Harrison, S., Kargel, J. S., Huggel, C., Reynolds, J., Shugar, D. H., Betts, R. A., Emmer, A., Glasser, N., Haritashya, U. K., Klimeš, J., Reinhardt, L., Schaub, Y., Wiltshire, A., Regmi, D., & Vilímek, V. (2018). Climate change and the global pattern of moraine-dammed glacial lake outburst floods. Cryosphere, 12(4), 1195–1209. https://doi.org/10.5194/tc-12-1195-2018

Hasnain, S. I, Jose P.G., Ahmad, S and Negi, D.C. 2001. Character of the subglacial drainage system in the ablation area of Dokriani glacier, India, as revealed by dye-tracer studies. Journal of Hydrology Vol. 248(1-4), pp.216-223.

Hock, R., Rasul, G., Adler, C., Cáceres, B., Gruber, S., Hirabayashi, Y., Jackson, M., Kääb, A., Kang, S., Kutuzov, S., Milner, A., Molau, U., Morin, S., Orlove, B., and Steltzer, H.: High Mountain Areas, in: IPCC Special Report on the Ocean and Cryosphere in a Changing Climate, edited by: Pörtner, H.-O., Roberts, D. C., Masson-Delmotte, V., Zhai, P., Tignor, M., Poloczanska, E., Mintenbeck, K., Alegriìa, A., Nicolai, M., Okem, A., Petzold, J., Rama, B., and Weyer, N.: High Mountain Areas, in: IPCC Special Report on the Ocean and Cryosphere in a Changing Climate, edited by: Pörtner, H.-O., Roberts, D. C., Masson-Delmotte, V., Zhai, P., Tignor, M., Poloczanska, E., Mintenbeck, K., Alegriìa, A., Nicolai, M., Okem, A., Petzold, J., and Rama, B. N. M., IPCC, 94 pp., 2019.

Huber, J., McNabb, R., & Zemp, M. (2020). Elevation Changes of West-Central Greenland Glaciers From 1985 to 2012 From Remote Sensing. Frontiers in Earth Science, 8(February), 1–16. https://doi.org/10.3389/feart.2020.00035

Hugonnet, R., McNabb, R., Berthier, E., Menounos, B., Nuth, C., Girod, L., Farinotti, D., Huss, M., Dussaillant, I., Brun, F., & Kääb, A. (2021). Accelerated global glacier mass loss in the early twenty-first century. Nature, 592(7856), 726–731. https://doi.org/10.1038/s41586-021-03436-z

Immerzeel, W. W., Droogers, P., M. de Jong, S. & Bierkens, M. F. P. (2009) Large-scale monitoring of snow cover and runoff simulation in Himalayan river basins using remote sensing, Remote Sens. Environ., 113, 40–49. https://doi:10.1016/j.rse.2008.08.010.

Immerzeel, W. W., Lutz, A. F., Andrade M., Bahl, A., Biemans, H., Bolch, T., Hyde, S., Brumby, S., Davies, B.J., Elmore, A.C., Emmer, A., Feng, M., Fernández, A., Haritashya, U., Kargel, J.S., Koppes, M., Kraaijenbrink, P.D.A., Kulkarni, A.V., Mayewski, P.A., Nepal, S., Pacheco, P., Painter, T.H., Pellicciotti, F., Rajaram, H., Rupper, S., Sinisalo, A., Shrestha, A.B., Viviroli, D., Wada, Y., Xiao, C., Yao, T., & Baillie, J.E.M. (2020) Importance and vulnerability of the world's water towers. Nature, 577(7790):364-369. https://doi: 10.1038/s41586-019-1822-y.

Jain, S.K., Goswami, A., & Saraf, A.K. (2008). Accuracy assessment of MODIS, NOAA and IRS data in snow cover mapping under Himalayan conditions. International Journal of Remote Sensing, 29(20), 5863–5878.

Kargel, J.S., Abrams, M.J., Bishop, M.P., Bush, A., Hamilton, G., Jiskoot, H., Kääb, A., Kieffer, H.H., Lee, E.M., Paul, F. (2005): Multispectral imaging contributions to global land ice measurements from space. Remote Sensing Environment. Volume. 99,pp.187–219.

Kaser, G., Cogley, J. G., Dyurgerov, M. B., Meier, M. F., & Ohmura, A. (2006). Mass balance of glaciers and ice caps: Consensus estimates for 1961-2004. Geophysical Research Letters, 33(19), 1–5. https://doi.org/10.1029/2006GL027511

Kulkarni A.V., 1992, Mass balance of Himalayan glaciers using AAR and ELA methods, Journal of Glaciology 38(128), 101-104.

Kulkarni, A. V., Bahuguna, I. M., Rathore, B. P., Singh, S. K., Randhawa, S. S., Sood, R. K., & Dhar, S. (2007). Glacial retreat in Himalaya using Indian Remote Sensing satellite data. Current Science, 92(1), 69–74. https://doi.org/10.1117/12.694004

Kumar, A., Negi, H. S., Kumar, K., Shekhar, C., & Kanda, N. (2019). Quantifying mass balance of East-Karakoram glaciers using geodetic technique. Polar Science, 19(November), 24–39. https://doi.org/10.1016/j.polar.2018.11.005

Mandal, A., Vishwakarma, B. D., Angchuk, T., Azam, M. F., Garg, P. K., & Soheb, M. (2024). Glacier mass balance and its climatic and nonclimatic drivers in the Ladakh region during 2000-2021 from remote sensing data. Journal of Glaciology. https://doi.org/10.1017/jog.2024.19

Mandal, A., Ramanathan, AL., Azam, M. F., Angchuk, T., Soheb, M., Kumar, N., Pottakkal, J. G., Vatsal, S., Mishra, S. and Singh, V. B. (2020) Understanding the interrelationships among mass balance, meteorology, discharge and surface velocity on Chhota Shigri Glacier over 2002–2019 using in situ measurements. Journal of Glaciology, 1–21. https://doi.org/10.1017/jog.2020.42

Maurer, J.M., Schaefer, J.M., Rupper, S., & Corley, A. (2019). Acceleration of ice loss across the Himalayas over the past 40 years. Science Advances, 5, eaav7266.

Mir, R. A. (2018) Recent changes of two parts of Kolahoi Glacier and its controlling factors in Kashmir basin, western Himalaya. Remote Sensing Applications: Society and Environment, 11, 265-281. https://doi.org/10.1016/j.rsase.2018.07.009.

Motschmann, A., Huggel, C., Muñoz, R. & Thür A. (. 2020) Towards integrated assessments of water risks in deglaciating mountain areas: water scarcity and GLOF risk in the Peruvian Andes. Geoenvironmental Disasters, 7(1):26. https://doi: 10.1186/s40677-020-00159-7.

Muhammad, S., Tian, L., & Nüsser, M. (2019). No significant mass loss in the glaciers of Astore Basin (North-Western Himalaya), between 1999 and 2016. Journal of Glaciology, 65(250), 270–278. https://doi.org/10.1017/jog.2019.5

Ohmura, A. (2011). Observed Mass Balance of Mountain Glaciers and Greenland Ice Sheet in the 20th Century and the Present Trends. Surveys in Geophysics, 32(4–5), 537–554. https://doi.org/10.1007/s10712-011-9124-4

Osmaston, H. (1994). The geology, geomorphology and Quaternary history of Zangskar. In Himalayan Buddhist Villages: Environment, Resources, Society, and Religious Life in Zangskar, Ladakh (Eds. 1).

Pandey, P., & Venkataraman, G. (2013). Changes in the glaciers of Chandra-Bhaga basin, Himachal Himalaya, India, between 1980 and 2010 measured using remote sensing. International Journal of Remote Sensing, 34(15), 5584–5597. https://doi.org/10.1080/01431161.2013.793464

Paul, F., Huggel, C., & Kääb, A. (2004). Combining satellite multispectral image data and a digital elevation model for mapping debris-covered glaciers. Remote Sensing of Environment, 89(4), 510–518. https://doi.org/10.1016/j.rse.2003.11.007

Pottakkal, J. G., Al. Ramanathan, V. B. Singh, P. Sharma, M. F. Azam and A. Linda (2014) Characterization of subglacial pathways draining two tributary meltwater streams through the lower ablation zone of Gangotri glacier system, Garhwal Himalaya, India. Current Science Vol. 107, No. 4, 613-621

Racoviteanu, A. E., Williams, M. W., and Barry, R. G. (2008) Optical remote sensing of glacier characteristics: a review with focus on the Himalaya. Sensors. Volume. VII No.V,pp.3355–3383.

Rai, P.K., Nathawat, M.S., Mohan, K. (2013) Glacier Retreat in Doda Valley, Zanskar Basin, Jammu & Kashmir, India Universal Journal of Geoscience 1(3): 139-149, DOI: 10.13189/ujg.2013.010304.

Rodríguez, E., Morris, C. S., & Belz, J. E. (2006). A global assessment of the SRTM performance. Photogrammetric Engineering and Remote Sensing, 72(3), 249–260. https://doi.org/10.14358/PERS.72.3.249

Shukla, A., Garg, P. K., & Srivastava, S. (2018). Evolution of glacial and high-altitude lakes in the Sikkim, Eastern Himalaya over the past four decades (1975-2017). Frontiers in Environmental Science, 6(JUL), 1–19. https://doi.org/10.3389/fenvs.2018.00081

Shukla, S., Kansal, M.L., & Jain, S.K. (2017). Snow cover area variability assessment in the upper part of the Satluj River Basin in India. Geocarto International, 32, 1285–1306.

Snehmani, Dharpure, J.K., Kochhar, I., et al. (2016). Analysis of snow cover and climatic variability in Bhaga basin located in western Himalaya. Geocarto International, 31, 1094–1107.

Tak, S. & Keshari, A. K. (2020) Investigating mass balance of Parvati glacier in Himalaya using satellite imagery based model. Scientific Reports, 10, 12211. https://doi.org/10.1038/s41598-020-69203-8

Tawde SA, Kulkarni AV and Bala G (2016) Estimation of glacier mass balance on a basin scale: an approach based on satellite-derived snowlines and a temperature index model. Curr. Sci., 111(12), 1977–1989 (doi: 10.18520/cs/v111/i12/1977-1989)

Taylor, P.J., & Mitchell, W.A. (2000). The Quaternary glacial history of the Zanskar Range, north-west Indian Himalaya. Quaternary International, 65–66, 81–99.

Vincent, C., Ramanathan, A., Wagnon, P., Dobhal, D. P., Linda, A., Berthier, E., Sharma, P., Arnaud, Y., Azam, M. F., Jose, P. G., & Gardelle, J. (2013). Balanced conditions or slight mass gain of glaciers in the Lahaul and Spiti region (northern India, Himalaya) during the nineties preceded recent mass loss. The Cryosphere, 7(2), 569–582. https://doi.org/10.5194/tc-7-569-2013

Wagnon, P., Linda, A., Arnaud, Y., Kumar, R., Sharma, P., Vincent, C., Pottakkal, J. G., Berthier, E., Ramanathan, A., Hasnain, S. I., & Chevallier, P. (2007). Four years of mass balance on Chhota Shigri Glacier, Himachal Pradesh, India, a new benchmark glacier in the western Himalaya. Journal of Glaciology, 53(183), 603–611. https://doi.org/10.3189/002214307784409306

Zemp, M., Frey, H., Gärtner-Roer, I., Nussbaumer, S. U., Hoelzle, M., Paul, F., Haeberli, W., Denzinger, F., Ahlstrøm, A. P., Anderson, B., Bajracharya, S., Baroni, C., Braun, L. N., Càceres, B. E., Casassa, G., Cobos, G., Dàvila, L. R., Delgado Granados, H., Demuth, M. N., … Vincent, C. (2015). Historically unprecedented global glacier decline in the early 21st century. Journal of Glaciology, 61(228), 745–762. https://doi.org/10.3189/2015JoG15J017

Zemp, M., Huss, M., Thibert, E., Eckert, N., McNabb, R., Huber, J., Barandun, M., Machguth, H., Nussbaumer, S. U., Gärtner-Roer, I., Thomson, L., Paul, F., Maussion, F., Kutuzov, S., & Cogley, J. G. (2019). Global glacier mass changes and their contributions to sea-level rise from 1961 to 2016. Nature, 568(7752), 382–386. https://doi.org/10.1038/s41586-019-1071-0

Zhang, Z., Liu, S., Zhang, Y., Wei, J., Jiang, Z., & Wu, K. (2018). Glacier variations at Aru Co in western Tibet from 1971 to 2016 derived from remote-sensing data. Journal of Glaciology, 64(245), 397–406. https://doi.org/10.1017/jog.2018.34